







RESEARCH ARTICLE | JULY 03 2024


Oscillating flow around a circular cylindrical post confined between two parallel plates

A. J. Bárcenas-Luque   ; F. Moral-Pulido  ; C. Gutiérrez-Montes  ; W. Coenen  ; C. Martínez-Bazán 




Physics of Fluids 36, 071903 (2024)

<https://doi.org/10.1063/5.0209927>



Physics of Fluids
Special Topic:
Flow and Climate
Guest Editors: Khaled Ghannam and Mostafa Momen
[Submit Today!](#)



Oscillating flow around a circular cylindrical post confined between two parallel plates

Cite as: Phys. Fluids **36**, 071903 (2024); doi: [10.1063/5.0209927](https://doi.org/10.1063/5.0209927)

Submitted: 24 March 2024 · Accepted: 14 June 2024 ·

Published Online: 3 July 2024



View Online



Export Citation



CrossMark

A. J. Bárcenas-Luque,^{1,2,a)} F. Moral-Pulido,^{3,4} C. Gutiérrez-Montes,^{3,4} W. Coenen,⁵ and C. Martínez-Bazán^{1,2}

AFFILIATIONS

¹Department of Mechanics of Structures and Hydraulic Engineering, University of Granada, 18001 Granada, Spain

²Andalusian Institute for Earth System Research, University of Granada, Avda. del Mediterráneo s/n, 18006 Granada, Spain

³Department of Mechanical and Mining Engineering, University of Jaén, 23071 Jaén, Spain

⁴Andalusian Institute for Earth System Research, University of Jaén, Campus de las Lagunillas, 23071 Jaén, Spain

⁵Department of Thermal and Fluid Engineering, University Carlos III of Madrid, 28911 Leganés, Spain

^{a)} Author to whom correspondence should be addressed: ajbarcenas@ugr.es

ABSTRACT

This work is motivated by the interest in determining the effect of the micro-anatomy of the spinal subarachnoid space (SSAS) on the cerebrospinal fluid flow. To that aim, we model the nerve roots in the SSAS by circular posts of radius a , confined between two parallel plates separated by a distance $2h$ and subjected to an oscillatory flow of angular frequency ω . First, we analyze the asymptotic limit of small values of the dimensionless stroke length of the oscillatory flow, for a harmonic waveform, varying the aspect ratio of the post $\lambda = h/a$ and the Womersley number $Wo = (a^2\omega/\nu)^{1/2}$. For low values of Wo , the time-averaged steady flow exhibits symmetric recirculating vortices attached to the wall of the post whose size decreases as Wo increases. However, for values of Wo larger than a critical one, $Wo_c(\lambda)$, which depends on λ , a second, outer vortex is also formed. The dependence of $Wo_c(\lambda)$ has been quantified in the range $0.5 < \lambda < \infty$, showing a decrease in Wo_c with λ . The analysis has been corroborated experimentally for $\lambda = 2$, and varying Wo , the stroke length as well as the wave form of the oscillating flow. Imposing an anharmonic oscillating flow shows that the fort-and-aft symmetry of the steady flow is broken, with the formation of two vortices of different size when $Wo < Wo_c$ and only one outer vortex in the systolic direction when $Wo > Wo_c$. Finally, the study is experimentally extended considering an array of equally spaced posts, separated a semi-distance $d = 2a$ aligned with the flow. Qualitatively, the steady flow patterns induced for $\ell = d/a = 2$ are similar to those for $\ell \rightarrow \infty$, although the presence of the nearby posts confines the recirculating vortices and delays the flow transition, increasing $Wo_c(\lambda)$.

Published under an exclusive license by AIP Publishing. <https://doi.org/10.1063/5.0209927>

I. INTRODUCTION

The spinal subarachnoid space (SSAS) forms an annular slender canal filled of cerebrospinal fluid (CSF) bounded externally by the dura membrane and internally by the pia membrane surrounding the spinal cord. Along it, CSF features an oscillatory velocity, mainly induced by the combined contribution of the cardiac and the respiratory cycles.^{1,2} The anatomy of the SSAS is known to present a complex geometry, including the presence of microanatomical elements,³ namely, trabeculae, denticulate ligaments, and nerve roots, across the width of the canal, that is much smaller than its perimeter and which, in turn, is much smaller than its length. In particular, nerve roots are present in most spinal segments and can be found on both sides of the canal arranged in bundles that emerge from the spinal cord and exit

the vertebral column through the intervertebral discs (see Fig. 1). These elements have been reported to play an important role in the transport of substances along the spinal canal,^{4–9} such as drugs injected intrathecally. The present paper, focused on a simplified geometry, is inspired by the study of the effect of such elements on the flow of CSF and the transport of solutes in the SSAS. Thus, taking into account the anatomy of the canal, the description of the effect of nerve roots in the SSAS can be approached, in a first approximation, as that of a flat canal in the presence of obstacles facing the oscillatory CSF flow (see Fig. 2). This configuration is used herein to elucidate the influence of these anatomical elements on the CSF flow, and more specifically on the mean, steady Lagrangian motion that is generated, and which is mainly responsible for the transport of solutes.¹⁰ The mean

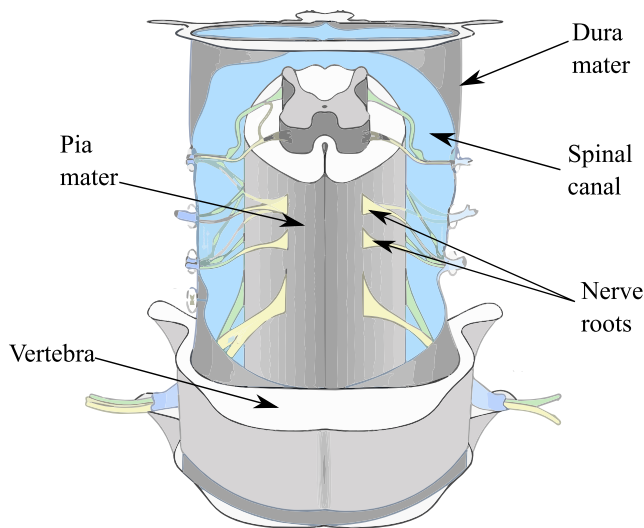


FIG. 1. Representation of the spinal canal with indication of the nerve roots across it.

Lagrangian velocity experienced by a fluid particle in the SSAS is the sum of the steady-streaming velocity, determined by time-averaging the Eulerian velocity field^{11,12} and the Stokes drift,¹³ a purely kinematic effect associated with the spatial nonuniformity of the pulsatile flow.

The phenomenon of steady or acoustic streaming, documented by Rayleigh¹⁴ in the last quarter of the 19th century, has been extensively studied since then and it is considered a classical fluid mechanics problem. It is known that an oscillating fluid stream, characterized by a velocity $U_\infty \cos(\omega t)$, interacting with a stationary solid body, leads to a time-averaged steady-streaming motion.¹¹ The resulting solution depends on the velocity amplitude, U_∞ , the object size, a , the oscillating angular frequency, ω , and the fluid's kinematic viscosity, ν . These parameters can be combined to give two dimensionless, controlling parameters, i.e., the dimensionless stroke length $\varepsilon = U_\infty/\omega a$, and the Womersley number $Wo = (a^2\omega/\nu)^{1/2}$, related to the Reynolds number by $Re = U_\infty a/\nu = \varepsilon Wo^2$. For $\varepsilon \ll 1$, the problem permits a theoretical description, where the velocity components are expressed as an asymptotic expansion involving powers of ε . The leading-order terms, satisfying convection-free linear equations, manifest as harmonic functions with zero time-averaged values, while the first-order corrections introduce a non-zero steady-streaming component.¹¹

In the case of two-dimensional oscillating flow around a circular cylinder of radius, a , much smaller than its length, Holtmark *et al.*¹⁵ derived an analytical description of the Eulerian velocity for $\varepsilon \ll 1$, reformulated in primitive variables in the Appendix. This analysis provided expressions for both the dominant harmonic velocity and the subsequent first-order velocity corrections, later refined by Chong *et al.*¹⁶ In the distinguished regime of $Wo \sim 1$, the magnitude of the resulting steady-streaming velocity is of the order of that of the Stokes drift,¹⁷ what requires to take into account both phenomena to fully describe the mean, steady Lagrangian flow. In this case, the symmetry of the problem yields identical recirculatory patterns in all four quadrants. More precisely, when Wo is smaller than a critical value, Wo_c , each quadrant displays a single vortex directed toward the cylinder along the oscillation axis. However, for larger values of Wo , an

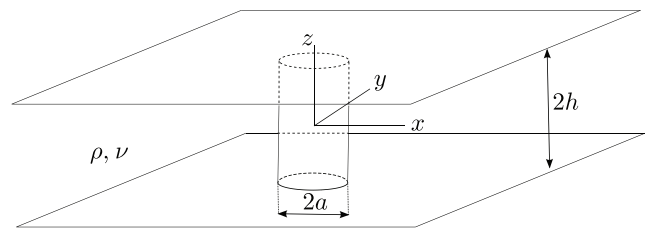


FIG. 2. Schematic configuration of the flow.

additional outer vortex is formed, a feature also confirmed by accompanying experiments.¹⁵ As Wo increases, the outer vortex strengthens while the inner one diminishes, being ultimately confined to a thin near-surface Stokes layer when $Wo \gg 1$. Similar flow characteristics have been observed when the flow is confined between two coaxial cylinders, with the inner one oscillating and the outer one fixed.¹⁸

In the early seventies, Tatsuno¹⁹ investigated experimentally the secondary flow induced by an oscillating circular cylinder confined radially for values of $Wo \sim 1$ and finite dimensionless stroke lengths ε , finding a behavior similar to that of Skavlem and Tjötta¹⁸ but different values of the critical parameters. While the oscillating flow for $\varepsilon \ll 1$ remains periodic and symmetric about the oscillation axis, the solution encountered when ε takes values that are not sufficiently small is known to be more complicated. The periodic viscous flow becomes unstable to axially periodic vortices above a critical value of ε that depends on Wo leading to an asymmetrical flow featuring vortex shedding. This symmetry breaking is apparent in the experiments of Tatsuno and Bearman,²⁰ who identified eight different regimes of flow and reported a three-dimensional instability along the axis of the cylinder for most of the regimes with turbulent motion arising as the Reynolds number $Re = \varepsilon Wo^2$ exceeded a critical value. Furthermore, Justesen²¹ carried out a numerical study of planar oscillating flow around a circular cylinder in the range of high Reynolds number and finite ε where, depending on the parameters values, several flow regimes that included vortex shedding were documented.

Extension to two-dimensional configurations with multiple (infinitely long) cylinders can also be found in the literature.^{22,23} Of particular interest to the case of CSF flow over a bundle of nerve roots is the array of cylinders considered by Alaminos *et al.*²³

Regarding three-dimensional streaming flows in confined geometries, flow visualization has shown that, in the distinguished limit of Womersley number of order unity with solid boundaries, depending on the boundary layer thickness, the confined case remains very similar to the two-dimensional one toward the central plane.^{24,25} In the same regime, measurements of the three-dimensional velocity field show apparent three-dimensional effects which cannot be ignored, except in the midplane where symmetry enforces no axial motion, i.e., null velocity in the cylinder's axis direction.²⁶ Also for Womersley number of order unity and streaming Reynolds numbers, $Re_s = \varepsilon^2 Wo^2 \ll 1$, when the boundary surface is a bubble excited acoustically confined between two parallel walls, experiments reveal that there are large axial displacements near the bubble,²⁷ which was also analytically reported later.²⁸ Similarly, three-dimensional streaming flows involving multi-curvature bodies have been also studied.²⁹

The objective of the present work is to delve into the complexities of an oscillating, viscous and incompressible flow around a circular

cylindrical post confined between two parallel flat plates, as depicted in Fig. 2. As mentioned above, the work is motivated by the effect of nerve roots crossing the SSAS (Fig. 1) on the CSF flow in the spinal canal. The radii of these nerve roots range between $a \sim 1.25\text{--}3\text{ mm}$,³⁰ and the width of the canal $h \sim 1.5\text{--}10\text{ mm}$,^{31,32} such that their aspect ratio, defined by $\lambda = h/a$, ranges $\lambda \sim 0.5\text{--}8$. Since the cardiac frequency is approximately 1 s^{-1} , and the viscosity of CSF is $0.7\text{ mm}^2\text{ s}^{-1}$, the Womersley number ranges between 3.7 and 9, approximately. In the cervical spine, where the time-averaged velocity over an oscillation period is approximately 1 cm s^{-1} , the dimensionless stroke length ε ranges 0.5–1.3, whereas in the lumbar spine, due to the much smaller velocities, on the order of 0.2 cm s^{-1} , the dimensionless stroke length ε is 0.1–0.25. To the best of our knowledge, situations where the obstacle is confined between parallel plates such that the aspect ratio $\lambda \sim 1\text{--}10$, for Womersley numbers $Wo \sim 1\text{--}10$, have not been explored before. Although the main focus of the present work resides in the effect of confinement in the transverse direction, two separate extensions are included to bridge the gap with the realistic case of CSF flow over a bundle of nerve roots: we consider an magnetic resonance imaging (MRI)-based anharmonic waveform of the flow rate, and we study an array of confined cylindrical posts. In contrast to the two-dimensional problem in Alaminos *et al.*,²³ here, we take into account the confinement suffered by the cylinder array, pinched between the pia and dura mater.

The paper is organized as follows. In Sec. II, an standard asymptotic analysis of steady-streaming flows for small stroke lengths, $\varepsilon \ll 1$, has been carried out together with the computation of the velocity correction or Stokes-drift. The numerical results are presented in Sec. III. In particular, the influence of the aspect ratio of the post on the streaming flow and the evaluation of the Lagrangian mean velocity field are reported in this section. Section IV is devoted to describe the complementary experiments performed, the results obtained being reported in Sec. V. Finally, concluding remarks, limitations, and future work are presented in Sec. VI.

II. FORMULATION

A fluid of density ρ and kinematic viscosity ν fills the gap between two infinite parallel plates separated by a distance $2h$ (see Fig. 2). Application of a uniform harmonic pressure gradient of angular frequency ω in a given direction x parallel to the plates results in a unidirectional motion with harmonic velocity \mathbf{v}' given by

$$\frac{\mathbf{v}'}{u_c} = \text{Re} \left\{ \text{ie}^{\text{i}\omega t'} \frac{\cosh \left[\left(\frac{1+\text{i}}{2} \right) h / \sqrt{\nu/\omega} \right] - \cosh \left[\left(\frac{1+\text{i}}{2} \right) z' / \sqrt{\nu/\omega} \right]}{\cosh \left[\left(\frac{1+\text{i}}{2} \right) h / \sqrt{\nu/\omega} \right] - 1} \right\} \mathbf{e}_x, \tag{1}$$

where t' and z' are the dimensional time and distance to the central plane, respectively, \mathbf{e}_x is the unit vector parallel to the pressure gradient, and u_c is the peak velocity amplitude, occurring at $z' = 0$. The exact solution (1) is altered by the presence of obstacles. We consider, in particular, the case of a circular cylinder perpendicular to the plates whose radius a is comparable to the inter-plate semidistance h , so that $\lambda = h/a \sim 1$. The description assumes frequencies ω comparable to the inverse of the viscous time $(a^2/\nu)^{-1}$ and stroke

lengths u_c/ω small compared with the cylinder radius a , as measured by the parameters

$$Wo = \left(\frac{a^2 \omega}{\nu} \right)^{1/2} \sim 1 \quad \text{and} \quad \varepsilon = \frac{u_c/\omega}{a} \ll 1. \tag{2}$$

Using ω , a , u_c , and $\rho u_c \omega a$ as scales for the time t , cartesian coordinates (x, y, z) , velocity $\mathbf{v} = (u, v, w)$, and spatial pressure difference p reduces the problem to that of integrating

$$\nabla \cdot \mathbf{v} = 0, \tag{3}$$

$$\frac{\partial \mathbf{v}}{\partial t} + \varepsilon \mathbf{v} \cdot \nabla \mathbf{v} = -\nabla p + \frac{1}{Wo^2} \nabla^2 \mathbf{v}, \tag{4}$$

for $x^2 + y^2 > 1$ and $-\lambda \leq z \leq \lambda$ subject to the nonslip boundary conditions

$$\mathbf{v} = 0 \begin{cases} \text{at } x^2 + y^2 = 1 & \text{for } -\lambda \leq z \leq \lambda, \\ \text{at } z = \pm \lambda & \text{for } x^2 + y^2 > 1, \end{cases} \tag{5}$$

and the far-field condition

$$\mathbf{v} = (\text{Re}[\text{ie}^{\text{i}t} U_0(z)], 0, 0) \quad \text{as } x^2 + y^2 \rightarrow \infty \quad \text{for } -\lambda \leq z \leq +\lambda, \tag{6}$$

where

$$U_0(z) = \frac{\cosh \left(\frac{1+\text{i}}{2} Wo \lambda \right) - \cosh \left(\frac{1+\text{i}}{2} Wo z \right)}{\cosh \left(\frac{1+\text{i}}{2} Wo \lambda \right) - 1}, \tag{7}$$

as follows from Eq. (1). In the limit $\varepsilon \ll 1$, the dependent variables can be expressed as expansions in powers of ε as follows:

$$\mathbf{v} = \mathbf{v}_0 + \varepsilon \mathbf{v}_1 + \dots \quad \text{and} \quad p = p_0 + \varepsilon p_1 + \dots \tag{8}$$

As can be anticipated from the two dimensional configuration, at the leading order in the limit $\varepsilon \ll 1$, the resulting motion is determined by a linear problem involving the balance of the local acceleration with the pressure and viscous forces. Convective acceleration will be seen to introduce a small relative correction of order ε , including a steady-streaming component, which is to be determined here.

A. Leading-order flow

The leading-order harmonic solution can be expressed in the form $\mathbf{v}_0 = \text{Re}[\text{ie}^{\text{i}t} \mathbf{V}]$ and $p_0 = \text{Re}[\text{e}^{\text{i}t} P]$, where $\mathbf{V}(x, y, z) = (U, V, W)$ and $P(x, y, z)$, by integration of

$$\nabla \cdot \mathbf{V} = 0, \tag{9}$$

$$-\mathbf{V} = -\nabla P + \frac{\text{i}}{Wo^2} \nabla^2 \mathbf{V}, \tag{10}$$

subject to the nonslip boundary conditions

$$\mathbf{V} = 0 \begin{cases} \text{at } x^2 + y^2 = 1 & \text{for } -\lambda \leq z \leq \lambda, \\ \text{at } z = \pm \lambda & \text{for } x^2 + y^2 > 1, \end{cases} \tag{11}$$

and the far-field condition

$$\mathbf{V} = [U_0(z), 0, 0] \quad \text{as } x^2 + y^2 \rightarrow \infty \quad \text{for } -\lambda \leq z \leq +\lambda. \quad (12)$$

B. Steady streaming

Collecting terms of order ϵ , the following order becomes

$$\nabla \cdot \mathbf{v}_1 = 0, \quad (13)$$

$$\frac{\partial \mathbf{v}_1}{\partial t} + \mathbf{v}_0 \cdot \nabla \mathbf{v}_0 = -\nabla p_1 + \frac{1}{Wo^2} \nabla^2 \mathbf{v}_1, \quad (14)$$

with boundary conditions

$$\mathbf{v}_1 = 0 \begin{cases} \text{at } x^2 + y^2 = 1 & \text{for } -\lambda \leq z \leq \lambda, \\ \text{at } z = \pm \lambda & \text{for } x^2 + y^2 > 1, \\ \text{as } x^2 + y^2 \rightarrow \infty & \text{for } -\lambda \leq z \leq \lambda. \end{cases} \quad (15)$$

The first-order corrections \mathbf{v}_1 and p_1 are 2π -periodic functions of time. As a result of the nonlinear interactions associated with the convective terms, their time-averaged values $\mathbf{v}_{SS} = \langle \mathbf{v}_1 \rangle$ and $p_{SS} = \langle p_1 \rangle$ are non-zero, with $\langle \cdot \rangle = \int_0^{2\pi} \cdot dt$ denoting the time-average operator. Taking the time average of (13)–(15) and using the identity $\langle \mathbf{v}_0 \cdot \nabla \mathbf{v}_0 \rangle = \frac{1}{2} \text{Re}[\mathbf{V} \cdot \nabla \mathbf{V}^*]$, where $*$ denotes complex conjugates, yields the steady-streaming problem

$$\nabla \cdot \mathbf{v}_{SS} = 0, \quad (16)$$

$$\frac{1}{2} \text{Re}[\mathbf{V} \cdot \nabla \mathbf{V}^*] = -\nabla p_{SS} + \frac{1}{Wo^2} \nabla^2 \mathbf{v}_{SS}, \quad (17)$$

with boundary conditions

$$\mathbf{v}_{SS} = 0 \begin{cases} \text{at } x^2 + y^2 = 1 & \text{for } -\lambda \leq z \leq \lambda, \\ \text{at } z = \pm \lambda & \text{for } x^2 + y^2 > 1, \\ \text{as } x^2 + y^2 \rightarrow \infty & \text{for } -\lambda \leq z \leq \lambda. \end{cases} \quad (18)$$

The steady-streaming velocity $\mathbf{v}_{SS} = \langle \mathbf{v}_1 \rangle$ provides the leading-order description for the mean Eulerian velocity $\langle \mathbf{v} \rangle = \epsilon \mathbf{v}_{SS}$ in the asymptotic limit $\epsilon \ll 1$.

C. Lagrangian mean motion

When addressing the oscillating flow around a cylinder, the Lagrangian mean motion of the fluid particles comes partly from the contribution of the Eulerian mean motion ($\mathbf{v}_{SS} = \langle \mathbf{v}_1 \rangle$) and partly from that of the so-called Stokes drift, arising in non-uniform oscillating flows. Consequently, streamlines visualized in experiments employing dyed fluid do not coincide in general with those determined from the steady-streaming velocity. The velocity of the Lagrangian mean motion is

$$\mathbf{v}_L = \mathbf{v}_{SS} + \frac{1}{2} \text{Im}(\mathbf{V} \cdot \nabla \mathbf{V}^*), \quad (19)$$

where $\frac{1}{2} \text{Im}(\mathbf{V} \cdot \nabla \mathbf{V}^*)$ corresponds to the Stokes drift contribution. Of particular interest is the role played by the complex function $\frac{1}{2} \mathbf{V} \cdot \nabla \mathbf{V}^*$ in determining the Lagrangian mean motion. In the steady streaming formulation, as discussed in (16) and (17), the forcing term is the real part of the complex function, while its imaginary part gives the Stokes-drift velocity. Notably, in the scenario of large Wo , viscous forces predominate within a thin Stokes layer. Beyond this layer, the flow is potential, characterized by the function \mathbf{V} being real. Consequently,

one can anticipate that the contribution of the Stokes drift is negligible in comparison with the steady-streaming one for large values of Wo .

III. NUMERICAL RESULTS

For $\lambda \sim 1$, no analytic solution is available, and the problem formulated in Sec. II must be solved numerically. To that aim, Eqs. (9) and (10) subject to (11) and (12) and Eqs. (16) and (17) subject to (18) were written in the weak form and implemented in the finite element solver COMSOL Multiphysics[®] v5.6 using the Weak Form PDE toolbox. In the regime herein investigated, i.e., $Wo \sim 1$ –10 and $\epsilon \ll 1$, the flow can be anticipated to be symmetric respect to the planes $y = 0$ and $z = 0$, and, thus, the computational domain for $y \geq 1$ and $z \geq 1$ has been considered imposing symmetry conditions in the aforementioned planes. The domain was discretized using a structured mesh with hexahedral elements. Second-order Lagrange elements were used for the pressure and the velocity. Mesh elements were compressed toward the solid and symmetry boundaries to assure enough spatial resolution. Both the domain extension and the mesh resolution were varied to assure the domain-size and grid-resolution independence of the results. In the final configuration, the typical element size ratio with respect to the radius, a , was ranged from 10^{-3} at the surfaces to 10^{-1} near the far-field boundary, assuring the accuracy of the solution with reasonable computational times. The domain extension in the x - and y -directions had a length of 25 times the radius of the cylinder, i.e., $25a$.

A. Steady streaming

There are different methods to represent and visualize a three-dimensional flow field. Some of these methods can be found in the literature (see, for instance, Refs. 33 and 34). In the cases of jet or wake-like flows, the Q -criterion or the λ_2 -criterion are widely accepted for the representation of the flow through vortical structures. When the exact analytical solution can be found, stream surfaces are often preferred to characterize the flow. In the particular case at hand, the absence of the normal component of the velocity field in the symmetry, $z = 0$ and $y = 0$, and antisymmetry planes, $x = 0$, and the fact that the symmetry of the flow is conserved when $\epsilon \ll 1$, allows the visualization of the flow topology by means of representation of the steady streaming streamfunction contours in these planes. Only one component of the vorticity field is not zero in each coordinate plane, so the corresponding streamfunction comes from $\nabla^2 \psi_{SS}^i = \Omega_{SS}^i$ for $i = 1(z = 0), 2(y = 0), 3(x = 0)$ with homogeneous Dirichlet boundary conditions in the far-field, in the cylinder and in the walls.

Representative results are shown in Fig. 3 for $Wo = 1, 12$, and 20 and for $\lambda = 0.5, 1$, and 5 . Because of the flow conditions and the geometrical configuration, the flow is symmetric respect to the plane $x = 0$. Therefore, only half of the domain ($x \geq 0$) is shown. The streaming structure arising for finite values of the dimensionless aspect ratio λ in the central plane $z = 0$ is qualitatively similar to that of a single cylinder ($\lambda \gg 1$). In this plane, the mean secondary Eulerian flow displays a vortex in each quadrant for the lower value of the Womersley number $Wo = 1$ (plotted in the left column), being the core of the vortex located along the $\pi/4$ ray and closer to the cylinder as λ decreases. This vortex is also known to progressively approach the post wall as Wo increases, as can be seen in Fig. 3 for $Wo = 1$ (left column), $Wo = 12$ (central column), and $Wo = 20$ (right column). These particular values of Wo have been selected to show the transition in

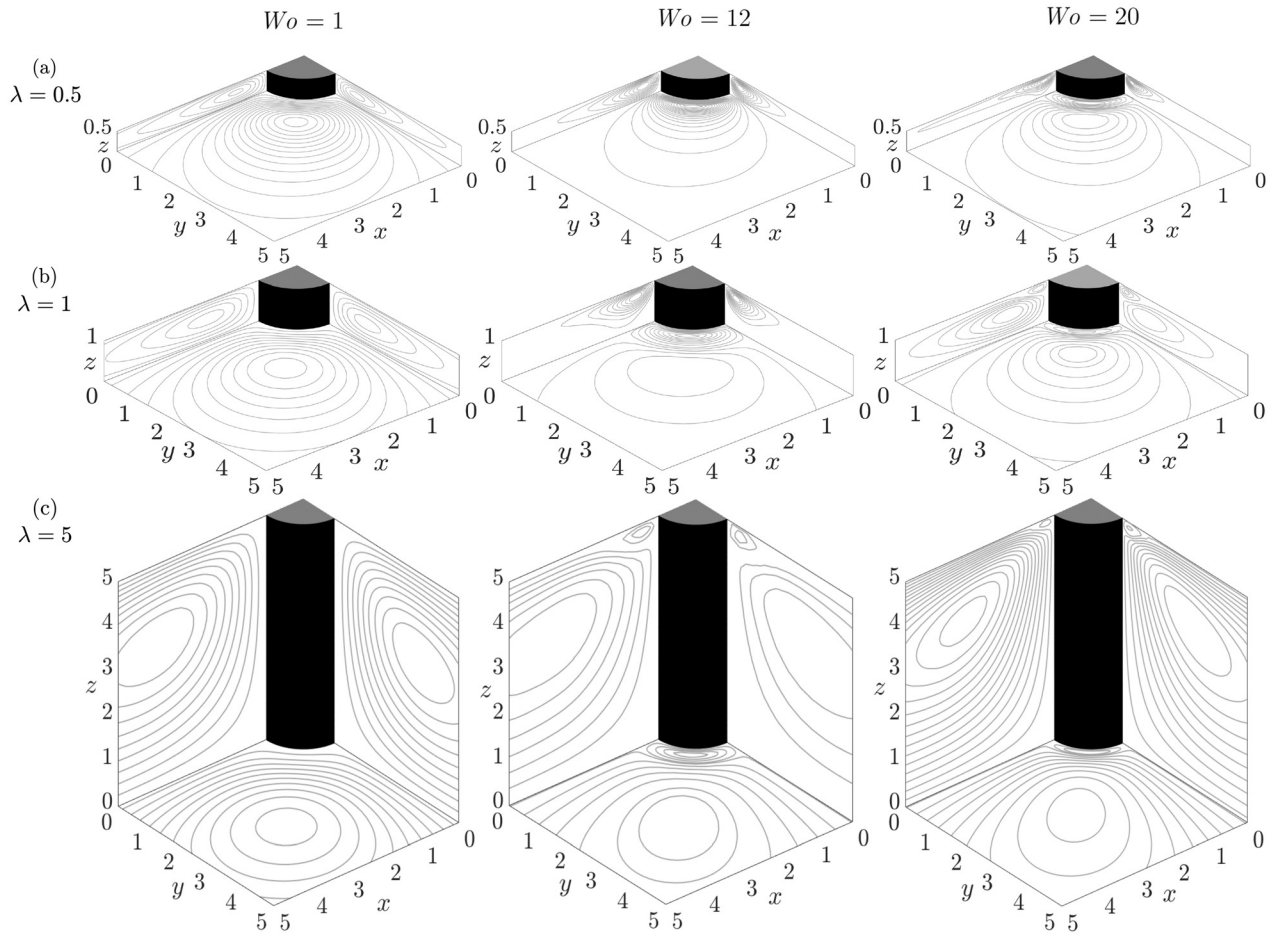


FIG. 3. Streamlines in the symmetry ($z = 0, y = 0$) and anti-symmetry ($x = 0$) planes corresponding to the steady-streaming velocity, v_{SS} , for $\lambda = 0.5$ (a), $\lambda = 1$ (b), and $\lambda = 5$ (c) for three different values of Wo .

the topology of the flow for the three values of λ , where a second vortex with opposite circulation begins to form outside when Wo exceeds a critical value, Wo_c . Thus, the critical value of the Womersley number, Wo_c , represents a threshold for which a change in the topology of the flow is observed.

As shown in Fig. 3, the critical value of the Womersley number depends on the aspect ratio λ . For $\lambda = 0.5$ [Fig. 3(a)], it can be seen that the transition occurs between $Wo = 12$ and $Wo = 20$, while for $\lambda = 1$ and $\lambda = 5$ the transition happens for $Wo < 12$ [Figs. 3(b) and 3(c)]. More details will be given below. In the planes $y = 0$ and $x = 0$, a similar behavior can be observed. As it happens in the plane $z = 0$, the vortex in each quadrant of these planes progressively approaches to the post as Wo increases. The core of these vortices is located at $z = \lambda/2$ for low values of Wo and it is situated at larger values of z , closer to the confining walls, when Wo increases. That indicates that the flow tends to be two-dimensional near the central plane ($z = 0$) for large values of Wo and for large values of λ . When the Womersley number, Wo , is increased sufficiently, a Stokes layer appears close to the solid boundaries and in the limit of $\varepsilon \ll 1, Wo \gg 1, Re_s \approx O(1)$, the flow outside this boundary layer becomes potential.

As previously indicated, the value of Wo_{cr} for which a change in flow topology occurs depends on λ . For the case of an infinite cylinder, $\lambda \gg 1$, the critical value of the Womersley number can be determined from the exact solution¹⁵ ($Wo_c \approx 6.08$) as the value of Wo for which the streamfunction ψ_{SS} vanishes in the far field. Our numerical simulations indicate that Wo_c varies with λ , increasing as λ decreases. This dependency is shown in Fig. 4, together with accompanying contours of the steady streaming functions in the central plane $z = 0$ for different pairs of Wo and λ , shown in the insets. The value of Wo_c is found to vary significantly for low values of λ . These higher values of Wo_c for lower values of λ are attributable to the effect of confinement, which also produces a drastic reduction in the magnitude of the streaming motion. In contrast, for sufficiently large values of λ , the value of Wo_c tends to that of the infinite cylinder (unconfined case). In this regard, as it can be seen for the cases of $\lambda = 1, 5, \infty$ with $Wo = 15$ in the three upper insets, the core of the outer vortex moves away from the post as the aspect ratio increases. Identical behavior is observed in the rest of the cases. Figure 4 also shows by a green point the value of Wo_c corresponding to the experimental configuration reported in Sec. IV.

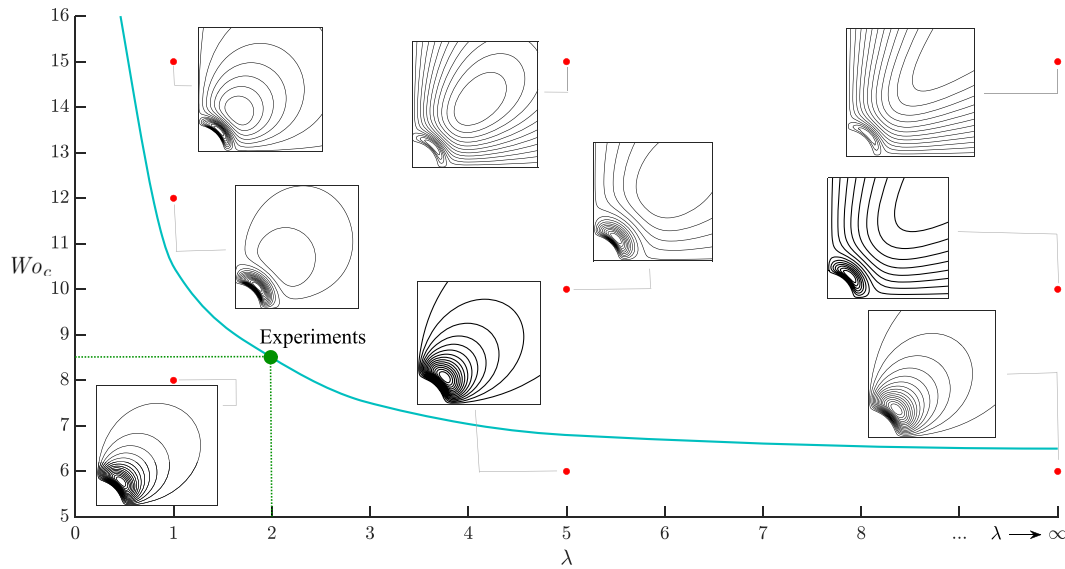


FIG. 4. Critical value of the Womersley number, Wo_c , as a function of λ . Insets show streamlines in the central plane, $z = 0$, for different values of Wo and λ . The green point indicates the value of Wo_c corresponding to the experimental configuration reported in Sec. IV.

B. Evaluation of the Lagrangian mean velocity

Figure 5 shows streamlines and color contours of vorticity Ω corresponding to three different velocity fields for $\lambda = 1$ and two Womersley numbers, i.e., $Wo = 0.5$ and $Wo = 12$. The first column shows the steady-streaming velocity, \mathbf{v}_{SS} , the second one the Stokes-drift or velocity correction, \mathbf{v}_{SD} , and the last one the steady mean Lagrangian velocity, given by the sum of the two of them, $\mathbf{v}_L = \mathbf{v}_{SS} + \mathbf{v}_{SD}$. Figure 5(a) displays streamlines and vorticity contours of the velocity fields in the symmetry planes $z = 0$ and $y = 0$ for $Wo = 0.5$, while in Fig. 5(b), the same results are presented for $Wo = 12$.

Regarding the streaming structure in the plane $z = 0$ for $Wo = 0.5$, the flow displays one vortex in each quadrant, with the clockwise circulation (negative vorticity) exhibited by the vortex in the first quadrant corresponding to fluid approaching the cylinder along the oscillation axis $y = 0$. In the plane $y = 0$, the flow, that is much weaker than in the middle symmetry plane $z = 0$, displays also one vortex in the semi-infinite space of $x > 1, y = 0$ with the identical behavior in the region of $x < -1, y = 0$. The Stokes-drift results for $Wo = 0.5$ display a primary clockwise-rotating vortex occupying most of the quadrant, along with a much weaker counter-rotating vortex of negligibly small circulation near the oscillation axis $y = 0$. For this value of Wo , this primary vortex is stronger than the corresponding steady-streaming vortex. The mean Lagrangian velocity field is largely determined by its Stokes-drift component, as reflected in the shape of the corresponding Lagrangian vortex in the right panel of Fig. 5(a).

As can be seen for $Wo = 12$ in Fig. 5(b), in the first quadrant of the center plane $z = 0$, the flow displays a second vortex with opposite circulation since Wo exceeds the corresponding critical value Wo_c for $\lambda = 1$ ($Wo_c \approx 10.2$), which in the case of Stokes-drift prevails over the inner vortex, similar to what happens in an array of cylinders.²³ The hegemony of the steady-streaming over the Stokes-drift in the mean Lagrangian motion becomes apparent in this range of the Womersley number. As inferred from Fig. 5, the Stokes drift prevails for

sufficiently small values of the Womersley number, whereas in the opposite limit the Stokes-drift motion fades away, as observed by comparing the steady-streaming and the mean Lagrangian motion contours, which are almost identical. Same dominance of the steady-streaming component happens in the plane $y = 0$, where no second vortex appears for this value of the Womersley number.

IV. EXPERIMENTS

The complementary experiments carried out allowed us to analyze the long-time-scaled flow patterns of the motion generated for different flow conditions, varying the frequency, the stroke volume of the oscillating flow, as well as the waveform. Two types of experiments were performed: the first one focused on the flow field around a single post and the second one on the flow around an array of five posts separated a distance $\ell = d/a$, where a is the radius of the posts and d the semi-distance between the axes of contiguous posts, being both types of experiments conducted in an adaptable experimental facility using distilled water of density $\rho = 998.2 \text{ kg/m}^3$ and kinematic viscosity $\nu = 10^{-6} \text{ m}^2/\text{s}$ as the working fluid. Figure 6(a) shows a sketch of the complete experimental facility, with the test section illuminated with a laser sheet, which includes the programmable pump used to establish the oscillating flow and the acquisition system. As seen in Fig. 6(b), the model consisted of an acrylic channel of total volume $V = 20 \times 10 \times 2 \text{ cm}^3$, where $L = 20 \text{ cm}$, $2w = 10 \text{ cm}$, and $2h = 2 \text{ cm}$ are the length, width, and height of the channel, respectively. The bottom of the channel was covered with black adhesive vinyl, which acted as a background for the experiments and at the same time prevented laser reflections. A vertical cylindrical post of radius $a = 5 \text{ mm}$ and length $2h = 2 \text{ cm}$, made of black anodized aluminum to minimized laser reflections, was perpendicularly placed at the center of the canal, being the corresponding aspect ratio $\lambda = h/a = 2$. Such radius was sufficiently small to avoid any influence from the lateral confining walls on the fluid motion near the post, being the distance between the axis of

31 July 2024 07:35:38

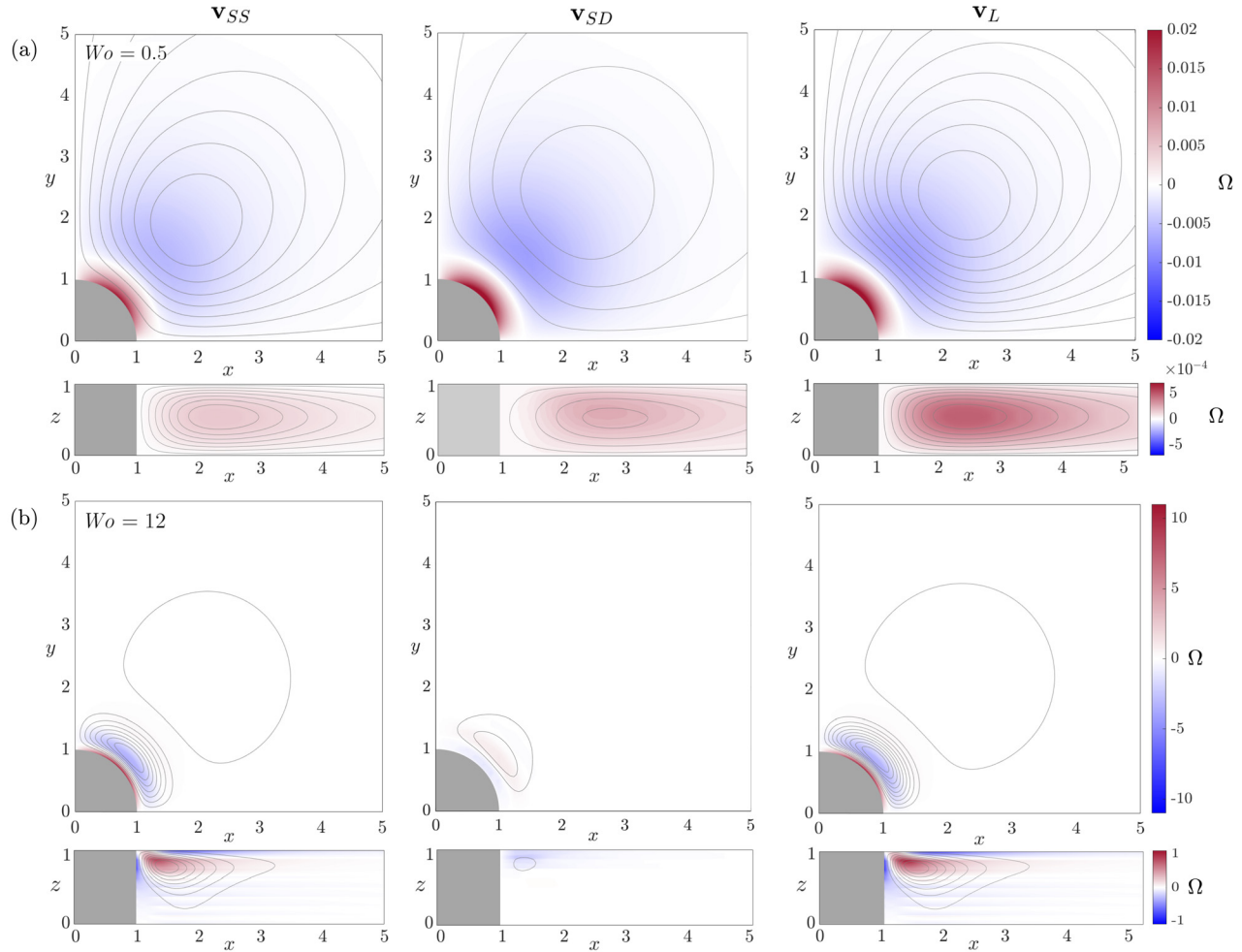


FIG. 5. Streamlines and color contours of vorticity Ω corresponding to the steady-streaming velocity, \mathbf{v}_{SS} , Stokes-drift velocity, \mathbf{v}_{SD} , and steady mean Lagrangian velocity, $\mathbf{v}_L = \mathbf{v}_{SS} + \mathbf{v}_{SD}$ for $\lambda = 1$ and $Wo = 0.5$ (a) and $Wo = 12$ (b). For each value of Wo , streamlines are represented using a constant spacing $\delta\psi = 0.01$ ($Wo = 0.5$) and $\delta\psi = 0.03$ ($Wo = 12$), with the corresponding vorticity levels indicated in the color bar on the right.

the post and the walls equal to $w = 10a$. This model configuration was also extended to consider a linear array of five posts, which were arranged aligned with the fluid motion. These elements were separated a distance $2d = 20$ mm, being the dimensionless inter-post semi-distance $\ell = d/a = 2$ since, for a typical diameter of a nerve root of $2a \sim 2.5\text{--}6$ mm and a separation distance of 3–10 mm,³⁰ in human beings the relevant values of ℓ ranges between 1 and 8. Thus, $\ell = 2$ falls within the characteristics physiological values. In both configurations, the posts were screwed to the bottom of the canal and perfectly anchored to the top surface. The *in vitro* model was connected to a CompuFlow 1000 MR programmable pump on one side, which generated the oscillatory flow with a prescribed waveform, and an open-air container on the other side, to allow the displacement of the stroke volume [see Fig. 6(a)]. Providing flow rate ranges, Q_{pump} , and oscillatory frequency ranges, f , between 0.1 and 35 ml/s with an accuracy of $\pm 3\%$ and 0.1–12 Hz, respectively, the pump allowed to vary the relevant parameters of the flow: the stroke volume, ΔV , the oscillatory

frequency, $f = \omega/(2\pi)$, and the waveform [from a harmonic sinusoidal wave to a MRI-based anharmonic one as displayed in Fig. 6(c)]. For this range of frequencies, the lowest Womersley number in the experiments was limited to $Wo \approx 5$. The fluid entered and exited the canal through two nozzles placed at the inlet and outlet sections, which also included flow conditioning elements to generate a uniform flow.

The experiments aimed at characterizing the time-averaged flow, induced by the oscillatory stream in the presence of the obstacles. To that end, in order to visualize the flow patterns and to measure the velocity and vorticity fields, particle image techniques were applied, seeding the flow with neutrally buoyant hollow glass spheres of diameter $\phi_p \approx 10 \mu\text{m}$. The experiments consisted of series of long-duration sequences of black-and-white images acquired in phase, at the same frequency as the oscillating flow. The sequences contained between 100 and 200 images depending on the experimental set, which were acquired with a CCD camera of resolution 2048×2048 pixels², equipped with a 50 mm Nikon lens to give a field of view of 38.9

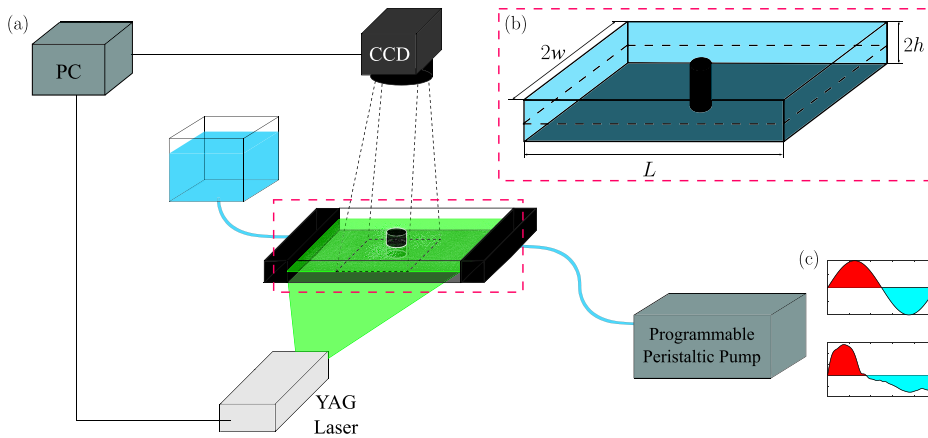


FIG. 6. (a) Schematic view of the experimental facility, consisting of the *in vitro* model, the pumping system (programmable peristaltic pump and opened-air container) and the image acquisition setup (Nd:YAG laser and CCD camera, both synchronized with a PC). (b) *In vitro* model with the corresponding dimensions. (c) Flow rate waveforms used in the experiments.

$\times 38.9 \text{ mm}^2$ for the sole post configuration, and $58.2 \times 58.2 \text{ mm}^2$ for the linear array configuration, providing a pixel resolution of 18.99 and $28.4 \mu\text{m}/\text{pixel}$, respectively. The camera was synchronized with a Nd:YAG dual-pulsed laser with a maximum pulse energy of 200 mJ able to run at a maximum frame rate of 15 Hz [Fig. 6(a)], used to generate a planar green sheet ($\lambda_{\text{laser}} = 541 \text{ nm}$) of width $\delta h < 1 \text{ mm}$ at $z = 0$ (streamwise direction—horizontal plane).

The resulting images were analyzed in two different ways to determine the fluid particle trajectories as well as the Lagrangian steady velocity and vorticity fields. To obtain the long-time-scaled Lagrangian trajectories, the images were first enhanced subtracting their background which was calculated using an average filter. Afterward, the steady fluid flow patterns could be extracted integrating all the snapshots acquired in each experimental set, to yield a cumulative image. It should be emphasized that all the images were taken at the same phase at a sampling frequency, f_s , equal to that of the oscillating flow, f . In addition, the velocity and vorticity fields were also determined using particle image velocimetry (PIV) analysis, applying the MATLAB toolbox PIVlab GUI³⁵ to couples of images acquired at an interval of time, $\Delta t = 1/f$. To perform the analysis, the images were first pre-processed, masking the cylinder to eliminate solid regions and applying a high-pass filter of window size larger than 150 pixels to avoid non-uniform background illumination, in combination with an automatic contrast adjustment. The PIV routine was applied to the pre-processed images, using an initial window of $160 \times 160 \text{ pixels}^2$ with a window reduction up to a minimal size of $32 \times 32 \text{ pixels}^2$ in four steps with a 50% overlap, providing a spatial resolutions of less than 0.5 mm in all the cases.

A series of experiments were conducted first to evaluate the effects of the Womersley number, Wo , and the dimensionless stroke volume, $\varepsilon = (U_\infty/\omega)/a$, where U_∞ is the amplitude of the oscillating flow, on the flow characteristics using a post with a fixed value of the aspect ratio $\lambda = 2$, complementing the numerical study reported in Sec. III. Thus, a value $\varepsilon = 0.2$ was initially established, assuming that it was small enough to approximate the distinguished limit $\varepsilon \ll 1$, and the Womersley number was varied from $Wo = 5$ to 11 (experimental sets 1–7 and 13–19 in Table I). Some of them will be compared with the numerical results reported in Sec. III. Then, the stroke volume was increased to $\varepsilon = 0.5$ to evaluate the effect of ε (experimental sets 8–12 and 20–23 in Table I). The experiments were performed considering

two different waveforms in order to investigate the effect of the shape of the flow rate on the induced flow patterns. The first waveform consisted of an harmonic function that provided a periodic flow rate given by $Q'(t') = Q_{\text{max}} \cos(\omega t')$, or similarly, a periodic velocity far from the post $u'_\infty(t') = U_\infty \cos(\omega t')$ with, $\omega = 2\pi f$, $u'_\infty(t') = Q'(t') / (4wh)$

TABLE I. Experimental conditions of the different sets of the experiments performed. Here, $Wo = (a^2\omega/\nu)^{1/2}$, $f = \omega/(2\pi)$, U_∞ is the peak velocity of the CSF motion for the harmonic waveform, and the harmonic equivalent peak velocity of the CSF motion for the anharmonic one, and $\varepsilon = (U_\infty/\omega)/a$. “Sine” indicates that the wave form is harmonic and “MRI” that is an anharmonic cardiac signal obtained from magnetic resonance imaging.

Experiment	Waveform	f (Hz)	Wo	U_∞ (mm/s)	ε
1	Sine	0.16	5	1.005	0.2
2	Sine	0.24	6	1.508	0.2
3	Sine	0.32	7	2.01	0.2
4	Sine	0.40	8	2.51	0.2
5	Sine	0.50	9	3.14	0.2
6	Sine	0.64	10	4.02	0.2
7	Sine	0.78	11	4.90	0.2
8	Sine	0.16	5	2.51	0.5
9	Sine	0.24	6	3.77	0.5
10	Sine	0.32	7	5.03	0.5
11	Sine	0.40	8	6.28	0.5
12	Sine	0.16	9	7.85	0.5
13	MRI	0.16	5	1.005	0.2
14	MRI	0.25	6	1.508	0.2
15	MRI	0.32	7	2.01	0.2
16	MRI	0.40	8	2.51	0.2
17	MRI	0.50	9	3.14	0.2
18	MRI	0.625	10	4.02	0.2
19	MRI	0.80	11	4.90	0.2
20	MRI	0.16	5	2.51	0.5
21	MRI	0.25	6	3.77	0.5
22	MRI	0.32	7	5.03	0.5
23	MRI	0.40	8	6.28	0.5

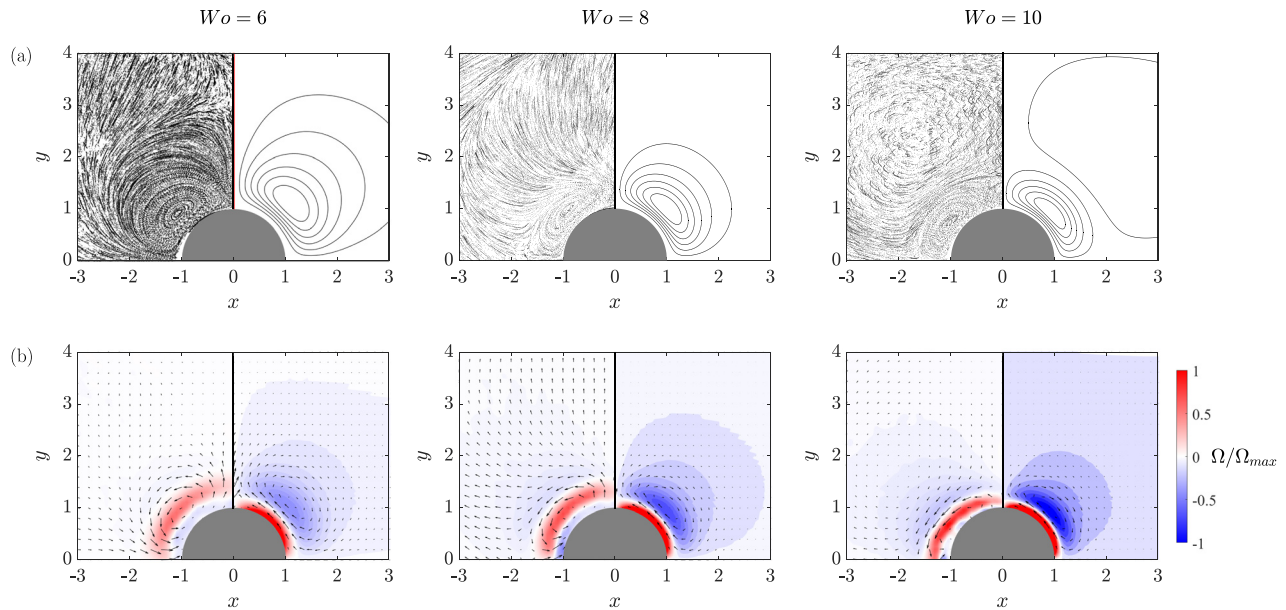


FIG. 7. (a) Steady pathlines and (b) normalized velocity field and vorticity contours of the flow around a single cylindrical post for $\varepsilon = 0.2$ and different values of Wo . Left side of each panel corresponds to the experimental measurements and right side to the analytical predictions ($\varepsilon \ll 1$). Colormap indicates the vorticity normalized with the overall maximum analytical and experimental values, respectively, Ω/Ω_{max} .

and $U_\infty = Q_{max}/(4wh)$ (experimental sets 1–12 in Table I). For the second waveform, a realistic anharmonic flow rate, obtained by MRI measurements, was used. This waveform, emulating the CSF motion along the spinal canal, was obtained by a modal Fourier analysis, using eight modes to produce a well fitted signal as described in Sec. VC (experimental sets 13–23 in Table I). Finally, additional experiments, not included in Table I, were conducted with a linear array of elements, aligned with the flow as described in Sec. VD.

V. EXPERIMENTAL RESULTS

In this section, the results of the time-averaged Lagrangian flow induced by the interaction of an oscillating stream with a single post and an array of posts obtained from the *in vitro* experiments are described. For the case of a single post, Sec. VA first discusses the effect of the Womersley number, Wo , for small values of the stroke length, $\varepsilon \simeq 0.2$, to be compared with numerical predictions of Sec. III, obtained for the limit $\varepsilon \ll 1$. These results are extended to order unity values of ε in Sec. VB, for which the asymptotic description in powers of ε , for $\varepsilon \ll 1$, is no longer valid. The analysis in Secs. VA and VB is conducted assuming a harmonic sinusoidal wave. In Sec. VC, this study is extended to analyze the time-averaged flow induced by an anharmonic oscillatory wave, similar to that found in realistic CSF flows, as induced by intracranial pressure fluctuations generated by the cardiac cycle. Finally, the time-averaged Lagrangian flow originated by the presence of an array of posts aligned with the flow oscillation axis is briefly described in Sec. VD.

A. Effect of flow frequency, Wo

As described in Sec. II, for small values of $\varepsilon \ll 1$, the motion can be decomposed into the sum of a zero-averaged purely oscillatory velocity field and a first-order correction, whose non-zero average is

denoted steady-streaming velocity. The Eulerian velocity field of the two-dimensional flow, $\lambda = \infty$, is described in the Appendix. Such description, although strictly valid for $\varepsilon \ll 1$, has been recently reported to provide results that remain reasonably accurate for finite values of ε , close to unity, for a linear array of circular cylinders.²³ Furthermore, the description of the long-timescale motion of a fluid particle includes the additional contribution of the Stokes drift¹⁶ that, in combination with the steady streaming, yields the mean Lagrangian velocity field. The Stokes drift has been found to be comparable to the steady streaming for $Wo \leq 1$, but negligible otherwise.³⁶ In the case at hand, since the values of Wo experimentally considered vary between 5 and 11, it is expected that the time-averaged Eulerian and Lagrangian velocity fields almost coincide in the cases reported in the present section for $\lambda = 2$.

In general terms, the results reveal that, as happens in the two-dimensional case, the Lagrangian mean motion in the horizontal symmetry plane $z = 0$ shows identical recirculation patterns in the four quadrants. Consequently, for the single post case, results in only one quadrant will be reported in the following (see Fig. 7). In this configuration, two different flow topologies can be identified. For values of the Womersley number below a critical one (denoted hereafter as subcritical values, $Wo < Wo_c$), a sole vortex forms in each quadrant (left panels in Fig. 7, $Wo = 6$), which, in the first quadrant, rotates in the clockwise direction, i.e., the flow moves toward the post along the stream’s oscillation axis, $y = 0$, and away from the post along the anti-symmetry axis, $x = 0$. For values larger than the critical one (or supercritical values), $Wo > Wo_c$, a secondary external counter-rotating vortex appears, which, differently from what happens in the two-dimensional flow, in this case is closed due to the presence of the confining walls (right panels in Fig. 7, $Wo = 10$). The external vortex encloses the internal one close to the wall of the post at distances that

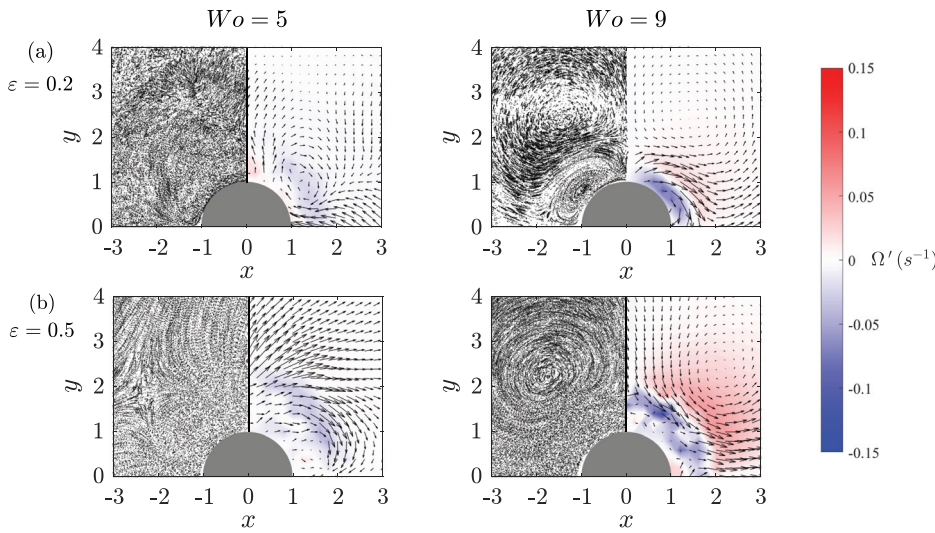


FIG. 8. Steady flow patterns (left side of each panel) and corresponding dimensional velocity and vorticity fields (right side of each panel) of the flow around a cylindrical element for $Wo < Wo_c$ (left column, $Wo=5$) and $Wo > Wo_c$ (right column, $Wo=9$). Here, (a) $\epsilon = 0.2$ is considered to satisfy the theoretical approximation ($\epsilon \ll 1$) and (b) $\epsilon = 0.5$ assumes to be of order-unity.

decrease as Wo increases. As indicated in Sec. III, the presence of the plates at the top and bottom boundaries has also an impact on the critical value, Wo_c , at which such flow topology change takes place. In particular, Wo_c increases as $\lambda = h/a$ decreases, being $Wo_c \simeq 6.08$ in the infinite cylinder case, $\lambda = \infty$, and $Wo_c \simeq 8.5$ in the present configuration, $\lambda = 2$ (see Fig. 4), which practically coincides with the value obtained analytically for $\epsilon \ll 1$. In addition, the numerical analysis shows that the time-averaged flow becomes three-dimensional, and it is characterized by the formation of two additional recirculating regions in the planes $x=0$ and $y=0$, although this issue will not be experimentally explored, due to optical access limitations. To illustrate these observations, Fig. 7 shows the comparison between the time-averaged analytical ($\epsilon \ll 1$) and experimental ($\epsilon \simeq 0.2$) results. In particular, Fig. 7(a) shows pathlines of the mean Lagrangian motion obtained experimentally, left or second quadrant, and analytically, right or first quadrant, for values of $Wo = 6, 8$, and 10 , in columns from left to right, respectively. The first two columns display flow topologies corresponding to $Wo < Wo_c$, whereas a change in the flow topology becomes apparent for $Wo = 10$, where a second external counter-rotating vortex appears, which confines the inner vortex to the high-vorticity Stokes layer close to the post. Figure 7(b) shows the vectors associated with the velocity fields, together with color contours of vorticity, normalized using the overall maximum analytical and experimental values of velocity and vorticity, respectively. In general terms, very similar and symmetric flow patterns are found for both the theoretical predictions and the measurements, with the analytical or experimental cores of the vortices located, approximately, along the $\pi/4$ or $3\pi/4$ rays, respectively, in all cases, the theory predicting slightly larger radial distances from the post to the vortex core. Finally, it can be also observed that increasing values of Wo yield more intense circulations, as inferred from the vorticity contours, while the core of the vortex, for $Wo < Wo_c$, and that of the internal vortex, for $Wo > Wo_c$, become closer to the post, as it was previously anticipated.

B. Effect of ϵ

The flow rate and stroke volume vary along the spinal canal, affecting the local value of ϵ , which also varies from order unity values

at the cervical region to very small values at the lower regions. The asymptotic description in powers of ϵ in the limit $\epsilon \ll 1$ ceases to be valid for finite values of the stroke length, $\epsilon \sim \mathcal{O}(1)$. To explore this effect, the experimental results for $\epsilon \sim \mathcal{O}(1)$ are shown herein for two values of Wo , namely, $Wo = 5 < Wo_c$ (sub-critical regime) and $Wo = 9 > Wo_c$ (supercritical regime), which are also compared with their counterparts for $\epsilon = 0.2$ (considered here to be a good representation of the distinguished limit $\epsilon \ll 1$). Therefore, Fig. 8 displays pathlines of time-averaged Lagrangian flow, left or second quadrant, and the corresponding velocity and vorticity fields, right or first quadrant, for $Wo = 5$, first column, and for $Wo = 9$, second column, for $\epsilon = 0.2$ in Fig. 8(a), and for $\epsilon = 0.5$ in Fig. 8(b). In this figure, the vorticity contours are shown with dimensions, Ω' to facilitate the comparison. In both Wo cases, similar flow patterns are observed for $\epsilon = 0.2$ and $\epsilon = 0.5$. Thus, a unique vortex is generated with clockwise rotation in the first quadrant for $Wo = 5$, whereas for $Wo = 9$, a second external counter-rotating recirculating region appears, enclosing the internal vortex near the post. A close inspection of the results reveals that increasing the stroke length has an impact on the global flow topology and rotation intensity. In that regard, for $Wo = 9$, the size of the vortices decrease as ϵ increases, and their cores move closer to the post. The latter is accompanied by more intense recirculations, as observed from the larger amplitudes of vorticity in the case of $\epsilon = 0.5$ compared to those of $\epsilon = 0.2$ in Fig. 8. These results agree with those recently reported by Alaminos-Quesada *et al.*²³

C. Time-averaged Lagrangian motion in anharmonic oscillating flows: CSF flow

So far, the analysis has been focused on the flow around a post subject to a harmonic stream flow of velocity $u'_\infty(t') = U_\infty \cos \omega t'$.

However, it is common to find oscillatory flows that present anharmonic temporal variations in nature, such as that of the blood in veins and arteries, or the CSF flow in the central nervous system (CNS).^{1,2} Therefore, in the present section, the study has been experimentally extended to analyze the flow induced by an anharmonic oscillatory flow around a post. Specifically, a wave of temporal dependence equal to that of a CSF flow measured in a human spinal canal³⁷

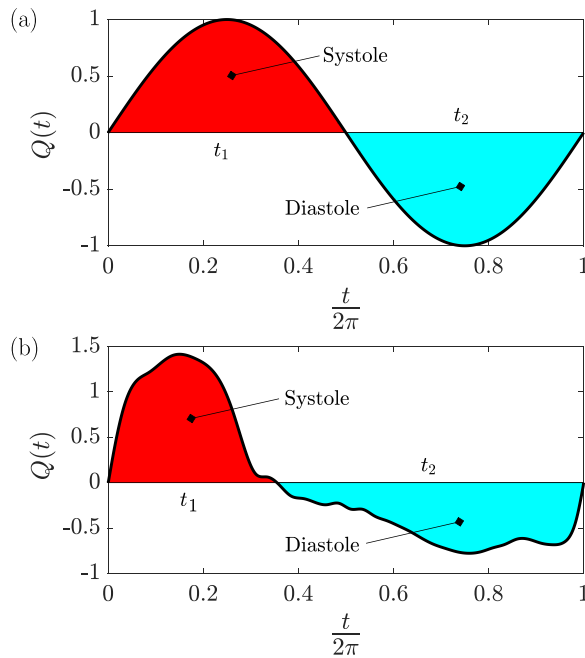


FIG. 9. (a) Harmonic flow waveform ($t_1 = t_2 = \pi$). (b) Realistic flow waveform, obtained through MRI measurements and set as Fourier expansion ($t_1 \neq t_2$). Here, $t = 2\pi t'/T$ represents the dimensionless time, with $T = 1/f = 2\pi/\omega$ as the period of the waveform.

has been considered. This velocity waveform can be expressed as a Fourier series $u'_\infty(t') = \sum_{n=1}^{\infty} \text{Re}[A_n e^{i(\omega_n t' + \phi_n)}]$, where A_n , ω_n , and ϕ_n are respectively the amplitude, angular frequency, and phase associated with each mode.^{23,38,39} Figure 9(a) shows the flow rate associated with a harmonic waveform, while Fig. 9(b) represents a period of the flow rate provided by a cardiac anharmonic waveform. In this figure, the positive and negative flow rates are given during systole, of dimensionless duration t_1 , and diastole, of dimensionless duration t_2 , respectively, with $\int_0^{2\pi} Q(t) dt = 0$ or, similarly, $|\int_0^{t_1} Q(t) dt| = |\int_{t_1}^{2\pi} Q(t) dt|$, where $t = 2\pi t'/T$ represents the dimensionless time, and $T = 1/f = 2\pi/\omega$ is the period of the waveform.

Unlike the results reported in Secs. V A and V B for the harmonic waveform where the secondary steady flow patterns were doubly symmetric, the flow induced by an anharmonic wave results in a steady motion which is only symmetric with respect to the axis of the flow oscillation $y=0$. Consequently, in the following, the first two quadrants, $y \geq 0$, of the plane $z=0$ will be shown to describe the flow. Figure 10(a) shows pathlines of the time-averaged Lagrangian flow for the harmonic wave, with their counterparts for the anharmonic wave shown in Fig. 10(b), both for $\varepsilon = 0.2$ and $Wo = 6, 8$, and 10 , respectively, where the first mode of the Fourier series, ω_1 , was used to define Wo in the anharmonic case and U_∞ has been defined as that of the equivalent harmonic waveform signal with the same period and stroke volume. As previously shown, the harmonic wave induces steady flow patterns that are symmetric in each quadrant. However, this symmetry is broken in the anharmonic case, as a result of the inter-modes interaction.^{23,39} For the lowest value of Wo ($Wo = 6$), the lack of fore-and-aft symmetry is already observable, where the vortices appear distorted,

with their cores near the post, as in the harmonic case. Despite this fact, differences can be observed in the size of the vortices, with the vortex located in the positive midplane ($x > 0$) being smaller than its complementary one in the negative one ($x < 0$). The loss of symmetry is also apparent for larger values of Wo , e.g., $Wo = 8$, where, as for $Wo = 6$, two vortices form close to the post with their cores displaced downward in the systolic direction (toward the positive x -coordinate). In addition, the two vortices seem to be surrounded by a region of fundamentally streamwise velocity, which becomes more noticeable for even larger values of Wo . It should be noted that, for $Wo = 10$, the flow topology has already changed. However, differently from the flow pattern observed when a harmonic waveform is imposed, where a second outer vortex is formed in each quadrant, the steady flow is characterized by the formation of only an outer vortex in the first quadrant (downstream in the systolic direction). Moreover, the two vortices, already present for $Wo < Wo_c$, undergo larger distortions and are also displaced downwards in the systolic direction. These three vortices are surrounded by an almost horizontal external stream, which is in agreement with the results obtained for the infinite cylinder⁴⁰ or more recently in a linear array of circular cylinders.²³

The effect of considering finite stroke lengths is analyzed in Fig. 11, where results for $\varepsilon = 0.5$ [Fig. 11(b)] are compared with those previously shown for $\varepsilon = 0.2$ [Fig. 11(a)], for $Wo = 6$ and 8 . As happened in the harmonic case, the size of the vortices formed is reduced when ε is increased, these being also more distorted and displaced downward in the systolic direction in this case. Interestingly, as it was previously anticipated, increasing ε has also an impact on the flow topology change, reducing the value of Wo_c . The latter can be observed for both values of Wo , for which only two vortices are formed close to the post when $\varepsilon = 0.2$, one in each quadrant, whereas a third external vortex appears when $\varepsilon = 0.5$ in the first quadrant already at $Wo = 6$.

D. Time-averaged motion around a linear array of posts

To further investigate the effect of the presence of different elements on the steady flow induced by an oscillatory stream flowing around them, the present section reports experimental results of the time-averaged Lagrangian flow around an array of five circular posts, aligned with the axis of oscillation, which are separated a semi-distance between the axes of contiguous posts d , with the dimensionless semi-distance $\ell = d/a = 2$.

Figure 12 shows time-averaged pathlines in the horizontal symmetry plane $z=0$ generated by a harmonic flow for different values of Wo , namely, $Wo = 5, 6$, and 9 , and two values of ε , i.e., $\varepsilon = 0.2$ [Fig. 12(a)] and 0.5 [Fig. 12(b)], for $\ell = 2$. Qualitatively, the steady flow patterns induced for $\ell = 2$ are similar to those for $\ell \rightarrow \infty$. Thus, considering the results for $\varepsilon = 0.2$, for $Wo = 5$ and 6 , two symmetric, counter rotating vortices are generated, one in each quadrant, with the same direction of rotation as for $\ell \rightarrow \infty$. The presence of contiguous posts renders a confining effect, limiting the size of each vortex to the semi-distance length in the axial direction. Consequently, deformed vortices are generated, whose cores are displaced toward the antisymmetry axis ($x=0$), in agreement with Ref. 23. This effect becomes more apparent for the lowest studied value of the Womersley number, $Wo = 5$, since the vortices reduce their size and move closer to the posts when Wo increases. The presence of neighboring posts also has an impact on Wo_c , delaying the flow transition featuring the apparition

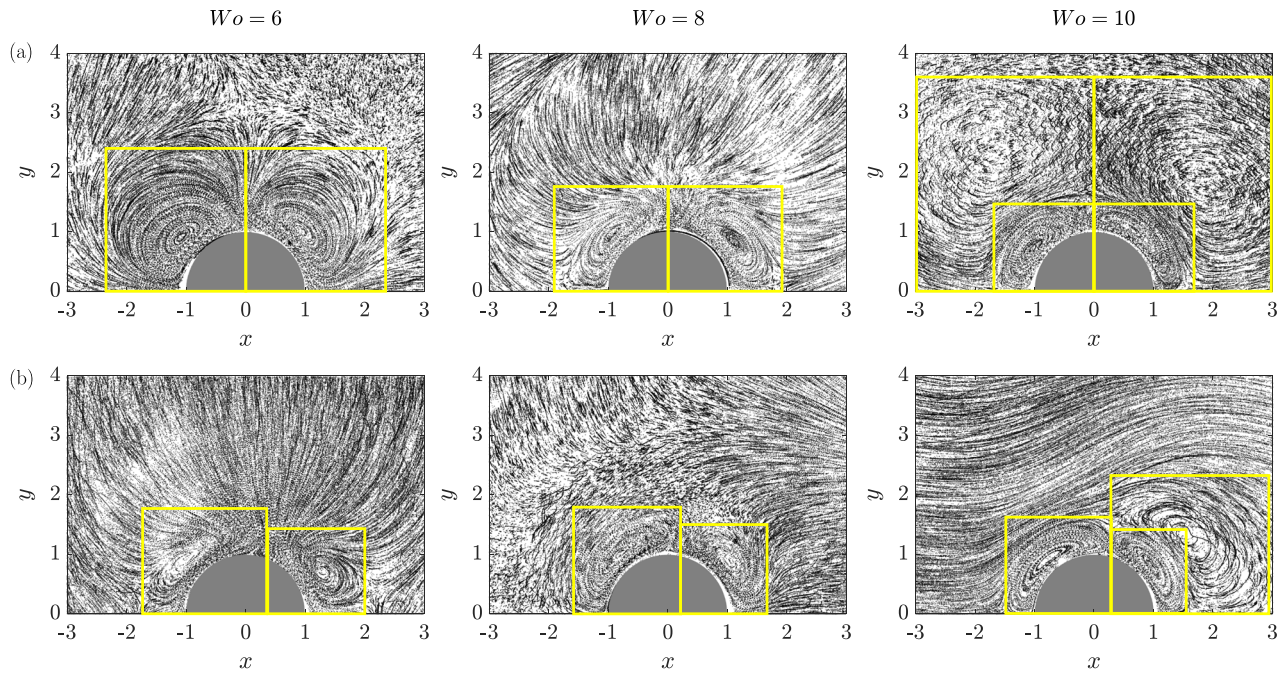


FIG. 10. Steady flow patterns around a cylindrical post of aspect ratio $\lambda = 2$ for $\epsilon = 0.2$ and different values of Wo using, a harmonic waveform (a) and an anharmonic one (b).

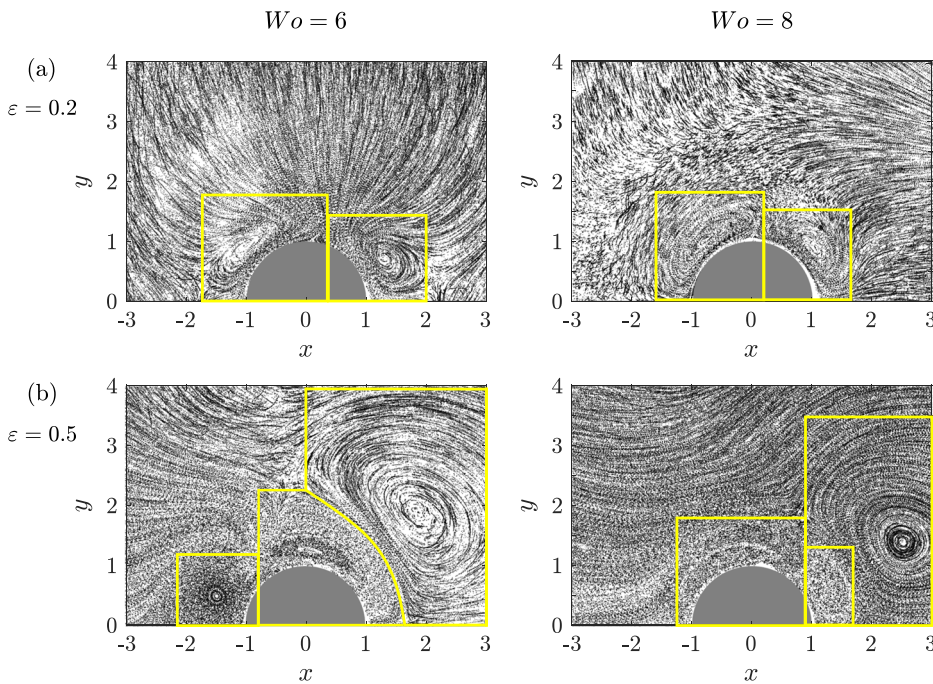


FIG. 11. Steady fluid particles trajectories around a cylindrical post of aspect ratio $\lambda = 2$ for $Wo = 6$ and 8 , obtained with an anharmonic, subject-specific CSF waveform. (a) $\epsilon = 0.2$ and (b) $\epsilon = 0.5$.

of external counter rotating vortices in each quadrant to larger values of Wo . The latter is noticeable for $Wo = 9$, where only two internal vortices are formed, one in each quadrant, whereas its counterpart for $\ell \rightarrow \infty$ displays two vortices in each quadrant ($Wo_c \simeq 8.5$ for

$\ell \rightarrow \infty$) as can be seen in Fig. 8. Figure 12(b) represents the results obtained for $\epsilon = 0.5$ for the same three values of Wo , also imposing a harmonic velocity. From an inspection of Fig. 12, it cannot be concluded that the size of the vortices substantially change with ϵ (at least

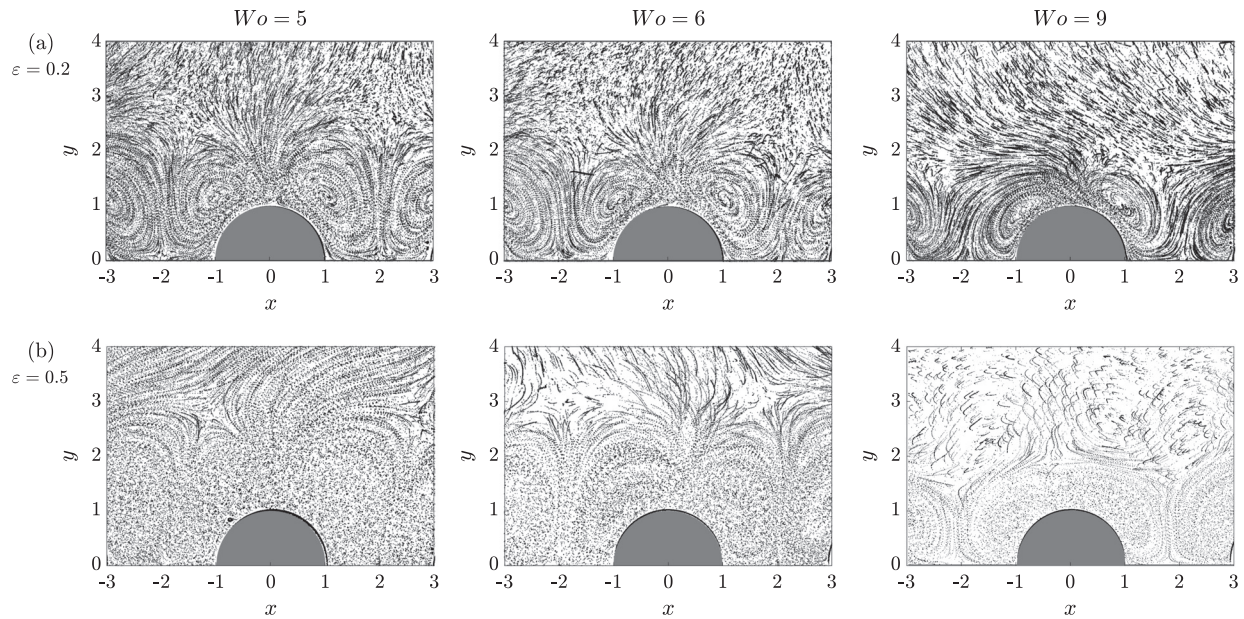


FIG. 12. Steady flow patterns around a linear array of cylindrical posts separated a semi-distance $\ell = 2$ at different values of Wo (columns) induced by a harmonic waveform for (a) $\varepsilon = 0.2$ and (b) $\varepsilon = 0.5$.

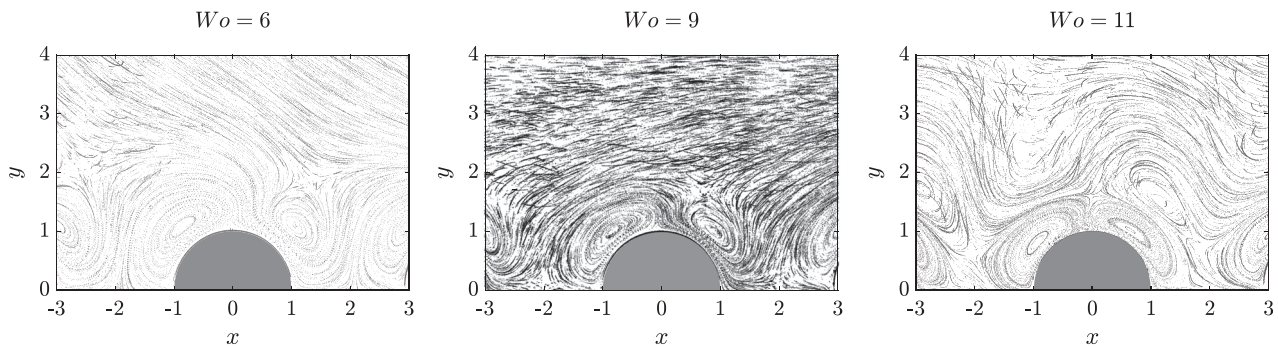


FIG. 13. Steady flow patterns around a linear array of cylindrical posts separated a semi-distance $\ell = 2$ for different values of Wo , induced by an anharmonic, patient-specific, waveform with $\varepsilon = 0.2$.

in the range of values of ε at which we have been able to perform the experiments). However, an increase in ε decreases the value of Wo_c , as it was commented in Secs. VB and VC. This can be observed in the case of $Wo = 9$, for which a pair of inner and outer counter rotating vortices are formed in each quadrant when $\varepsilon = 0.5$, whereas only an inner vortex is seen when $\varepsilon = 0.2$. The linear array configuration is further explored in Fig. 13, where time-averaged pathlines induced by an anharmonic fluid stream are shown for three values of Wo , two of them in the sub-critical regime ($Wo = 6$ and 9), and the other one in the supercritical regime ($Wo = 11$), all of them at $z = 0$ and for $\varepsilon = 0.2$. These kinds of waveforms have been found to cause the loss of flow symmetry in all quadrants; thus, this flow is only symmetric respect to the axis $y = 0$. As a consequence, for $Wo < Wo_c$, two different and asymmetric inner vortices are induced, with their cores unevenly displaced in the axial direction, which decrease in shape,

become closer to the posts and increase in intensity when Wo increases. For $Wo > Wo_c$, a second external vortex appears in the first quadrant, similar to what happened for $\ell \rightarrow \infty$, but in the case of $\ell = 2$, the vortices are deformed and axially enclosed within the semi-distance length. Moreover, in all cases, the vortices are also surrounded by a region of streamwise velocity.

VI. CONCLUSION

In this work, the problem of oscillatory streams around a cylindrical post, confined between two parallel plates, has been addressed. Eulerian and time-averaged Lagrangian flow fields have been described in detail for $\lambda = \mathcal{O}(1)$ and stroke volumes $\varepsilon < 1$. The problem has been initially tackled analytically and numerically for $\varepsilon \ll 1$, varying the Womersley number, Wo , and the post aspect ratio, λ . The numerical results indicate that, when the oscillating flow is harmonic, for a

given value of λ , at low values of Wo the flow field is sub-critical, showing a recirculating vortex anchored to the post symmetric with respect to the x and y axes. The size of the vortex decreases as λ decreases due to the confining effect of the upper and lower walls, at the same time that it narrows and approaches the surface of the post as Wo increases. However, for values of Wo larger than a critical one, $Wo_c(\lambda)$, which depends on λ , the flow becomes supercritical, with the formation of a second, outer vortex also symmetric, whose size decreases as λ decreases. The evolution of the critical Womersley number with the post aspect ratio is shown Fig. 4, with examples of the flow topology displayed for different values of λ and Wo . It can be clearly observed that transition between sub-critical and supercritical regimes is delayed when λ decreases, i.e., when the distance between the upper and lower walls is decreased, and the magnitude of the streaming motion is reduced. Regarding the Lagrangian mean motion, given by the sum of the steady-streaming and the Stokes drift, it can be concluded that the Stokes drift prevails over the steady-streaming for sufficiently small values of the Womersley number, whereas in the opposite limit, the Stokes-drift motion fades away. Nevertheless, for the range of interest of Wo in the present work, it has been observed that the steady-streaming dominates over the Stokes-drift.

The numerical results have been complemented by an experimental study, which compares the effect of Wo in the Lagrangian steady flow patterns at $z = 0$ and for $\lambda = 2$, showing a good agreement. This experimental work has been extended to situations beyond the theory, where ε is no longer much smaller than one, and cases close to reality, comparing the flow patterns obtained with harmonics and anharmonic waveforms. Furthermore, the mean Lagrangian flow generated by the presence of an array of posts immersed in an oscillatory stream has also been experimentally characterized, emulating the presence of nerve roots in the spinal subarachnoid space. Results obtained for a harmonic flow show time-averaged flow patterns that are identical in all quadrants, in each of which a recirculation cell forms near the post, for $Wo < Wo_c$, whose size reduces as Wo increases. When $Wo > Wo_c$, the flow topology changes, and a second, external vortex is formed. The time-averaged flow induced by an anharmonic waveform is found to lose the symmetry respect to the transversal axis, and two vortices of different size are formed at each side of the post in the sub-critical regime ($Wo < Wo_c$). However, in the supercritical regime ($Wo > Wo_c$), only an outer cell generates in the quadrant downstream, in the systolic direction. Regardless the waveform, the flow topology transition has been found to also depend on the stroke length ε , taking place at values of Wo_c that decrease as ε increases. Finally, considering a linear array of posts, the induced flow patterns are similar to those observed with a single post configuration when the stream is harmonic. However, significantly different flow topologies are found for anharmonic waveforms. These results aim to provide a better understanding of the characterization of the influence of microanatomy on CSF flow and lay the foundation for future research, where not only the fluid flow but also the solute transport should be taken into account.

ACKNOWLEDGMENTS

This work was supported by the coordinated project, PID2020-115961RB-C31, PID2020-115961RB-C32, and PID2020-115961RA-C33, financed by MICIU/AEI/10.13039/501100011033. F. Moral-Pulido wants to thank the Spanish Ministry of Universities

for the financial support provided by the Fellowship FPU18/05694. Fruitful discussions with Professor Antonio L. Sanchez are greatly acknowledged.

AUTHOR DECLARATIONS

Conflict of Interest

The authors have no conflicts to disclose.

Author Contributions

Antonio José Bárcenas-Luque: Conceptualization (equal); Data curation (equal); Formal analysis (equal); Investigation (equal); Visualization (equal); Writing—original draft (equal); Writing—review & editing (equal). **Francisco Moral-Pulido:** Conceptualization (equal); Data curation (equal); Formal analysis (equal); Investigation (equal); Writing—original draft (equal). **Cándido Gutiérrez-Montes:** Conceptualization (equal); Data curation (equal); Funding acquisition (equal); Investigation (equal); Resources (equal); Supervision (equal); Writing—original draft (equal); Writing—review & editing (equal). **Wilfried Coenen:** Conceptualization (equal); Formal analysis (equal); Funding acquisition (equal); Investigation (equal); Writing—original draft (equal); Writing—review & editing (equal). **Carlos Martínez-Bazán:** Conceptualization (equal); Data curation (equal); Funding acquisition (equal); Investigation (equal); Methodology (equal); Resources (equal); Supervision (equal); Writing—original draft (equal); Writing—review & editing (equal).

DATA AVAILABILITY

The data that support the findings of this study are available from the corresponding author upon reasonable request.

APPENDIX: REVISTING TWO-DIMENSIONAL STREAMING FLOW OVER A CIRCULAR CYLINDER

Using the same scales as the three dimensional problem for the time t , cartesian coordinates (x, y) , velocity $\mathbf{v} = (u, v)$, and spatial pressure difference p reduce the problem to that of integrating

$$\nabla \cdot \mathbf{v} = 0, \quad (\text{A1})$$

$$\frac{\partial \mathbf{v}}{\partial t} + \varepsilon \mathbf{v} \cdot \nabla \mathbf{v} = -\nabla p + \frac{1}{Wo^2} \nabla^2 \mathbf{v}, \quad (\text{A2})$$

for $x^2 + y^2 > 1$, subject to the nonslip boundary conditions

$$\mathbf{v} = 0 \quad \text{at} \quad x^2 + y^2 = 1, \quad (\text{A3})$$

and the far-field condition

$$\mathbf{v} = (\cos t, 0) \quad \text{as} \quad x^2 + y^2 \rightarrow \infty. \quad (\text{A4})$$

1. Eulerian velocity for $\varepsilon \ll 1$

Following standard practice, we describe the flow by introducing expansions for the different flow variables in powers of ε , i.e.,

$$\mathbf{v} = \mathbf{v}_0 + \varepsilon \mathbf{v}_1 + \dots, \quad (\text{A5})$$

and $p = p_0 + \varepsilon p_1 + \dots$. The leading-order solution satisfies the linear equation

$$\nabla \cdot \mathbf{v}_0 = 0, \tag{A6}$$

$$\frac{\partial \mathbf{v}_0}{\partial t} = -\nabla p_0 + \frac{1}{Wo^2} \nabla^2 \mathbf{v}_0, \tag{A7}$$

subject to boundary conditions stated in (A3) and (A4). The problem can be alternatively written using $\mathbf{v}_0 = \text{Re}(e^{it} \mathbf{V}_0)$ with $\mathbf{V}_0(x, y) = (U_0, V_0)$ representing a complex velocity. The integration can make use of the stream function $\Psi_0(x, y)$ defined such that

$$U_0 = \frac{\partial \Psi_0}{\partial y} \quad \text{and} \quad V_0 = -\frac{\partial \Psi_0}{\partial x}, \tag{A8}$$

and

$$\Omega_0 = -\nabla^2 \Psi_0, \tag{A9}$$

where the complex function $\Omega_0(x, y)$, related to the vorticity by

$$\omega_0 = \frac{\partial v_0}{\partial x} - \frac{\partial u_0}{\partial y} = \text{Re}(e^{it} \Omega_0), \tag{A10}$$

satisfies

$$iWo^2 \Omega_0 = \nabla^2 \Omega_0, \tag{A11}$$

as follows from (A7). Equations (A9) and (A11) must be integrated subject to

$$\Psi_0 = (x, y) \cdot \nabla \Psi_0 = 0 \quad \text{at} \quad x^2 + y^2 = 1, \tag{A12}$$

$$\frac{\partial \Psi_0}{\partial y} - 1 = \frac{\partial \Psi_0}{\partial x} = 0 \quad \text{as} \quad x^2 + y^2 \rightarrow \infty. \tag{A13}$$

For a general value of Wo , the resulting velocity $\mathbf{V}_0(x, y) = (U_0, V_0)$ has real and imaginary parts. Note, however, that in the limit of steady creeping flow $Wo \ll 1$, the solution is real everywhere, while in the inviscid limit $Wo \gg 1$, the solution contains an imaginary part only in the thin Stokes layer of thickness $1/Wo$ that develops on the cylinder surface, outside of which $\Omega_0 = 0$ and $\text{Im}(\mathbf{V}_0) = 0$.

Formulating the problem in cylindrical polar coordinates instead of Cartesians and separating variables, i.e., $\Omega_0(r, \theta) = \Omega_R(r)\Omega_\Theta(\theta)$, we find the following solution of Eq. (A11),

$$\Omega_0(r, \theta) = \frac{\pi}{2} \Omega i H_1^{(1)}(\alpha Wo r) \sin \theta, \tag{A14}$$

where Ω is a constant to be determined by the boundary conditions, $H_1^{(1)}$ is the Hankel function of first kind and order one and $\alpha = \sqrt{i}$.

Using the fact that Eq. (A9) is linear, it can be applied the superposition principle.

$$\nabla^2 \Psi_0 = -\Omega_0 : \begin{cases} \nabla^2 \hat{\Psi}_0 = 0 & \text{with b.c. (A12) - (A13),} \\ \nabla^2 \tilde{\Psi}_0 = -\Omega_0 & \text{with homogeneous b.c.} \end{cases} \tag{A15}$$

The solution of $\nabla^2 \hat{\Psi}_0 = 0$ with the boundary conditions (A12) and (A13) can be expressed as follows:

$$\hat{\Psi}_0 = A \left(r + \frac{B}{r} \right) \sin \theta, \tag{A16}$$

that has the same form as potential solution for the flow. The value of the constants of integration A and B will be determined below.

The equation $\nabla^2 \tilde{\Psi}_0 = -\Omega_0$ is solved using the Frobenius method, yielding

$$\tilde{\Psi}_0 = \frac{1}{\alpha M} \frac{H_1^{(1)}(\alpha Wo r)}{H_0^{(1)}(\alpha Wo)} \sin \theta. \tag{A17}$$

The leading order stream function will be

$$\Psi_0 = \hat{\Psi}_0 + \tilde{\Psi}_0. \tag{A18}$$

In this case, the stream function will be

$$\Psi_0 = \left[\frac{1}{\alpha Wo} \frac{H_1^{(1)}(\alpha Wo r)}{H_0^{(1)}(\alpha Wo)} - \frac{1}{2} \left(r + \frac{1}{r} \frac{H_2^{(1)}(\alpha Wo)}{H_0^{(1)}(\alpha Wo)} \right) \right] \sin \theta. \tag{A19}$$

To calculate the constant Ω it must be imposed the no slip boundary condition for the azimuthal velocity ($v_{\theta 0} = -\frac{\partial \Psi_0}{\partial r} = 0$ at $r = 1$). The value of the constant Ω in Eq. (A14) is

$$\Omega = \frac{H_2^{(1)}(\alpha Wo)}{H_0^{(1)}(\alpha Wo)}. \tag{A20}$$

As follows from collecting terms of order ϵ , the problem at the following order becomes

$$\nabla \cdot \mathbf{v}_1 = 0, \tag{A21}$$

$$\frac{\partial \mathbf{v}_1}{\partial t} + \mathbf{v}_0 \cdot \nabla \mathbf{v}_0 = -\nabla p_1 + \frac{1}{Wo^2} \nabla^2 \mathbf{v}_1, \tag{A22}$$

with boundary conditions

$$\mathbf{v}_1 = 0 \begin{cases} \text{at} & x^2 + y^2 = 1, \\ \text{as} & x^2 + y^2 \rightarrow \infty. \end{cases} \tag{A23}$$

The first-order corrections \mathbf{v}_1 and p_1 are 2π -periodic functions of time. As a result of the nonlinear interactions associated with the convective terms, their time-averaged values $\langle \mathbf{v}_1 \rangle$ and $\langle p_1 \rangle$ are non-zero, with $\langle \cdot \rangle = \int_0^{2\pi} \cdot dt$ denoting the time-average operator. Taking the time average of (A21)–(A23) and using the identity $\langle \mathbf{v}_0 \cdot \nabla \mathbf{v}_0 \rangle = \frac{1}{2} \text{Re}(\mathbf{V}_0 \cdot \nabla \mathbf{V}_0^*)$, where the asterisk $*$ denotes complex conjugates, provides the steady-streaming problem

$$\nabla \cdot \langle \mathbf{v}_1 \rangle = 0, \tag{A24}$$

$$\frac{1}{2} \text{Re}(\mathbf{V}_0 \cdot \nabla \mathbf{V}_0^*) = -\nabla \langle p_1 \rangle + \frac{1}{Wo^2} \nabla^2 \langle \mathbf{v}_1 \rangle, \tag{A25}$$

with boundary conditions

$$\langle \mathbf{v}_1 \rangle = 0 \begin{cases} \text{at} & x^2 + y^2 = 1, \\ \text{as} & x^2 + y^2 \rightarrow \infty. \end{cases} \tag{A26}$$

Introducing the time-averaged stream function $\langle \psi_1 \rangle$, with

$$\langle u_1 \rangle = \frac{\partial \langle \psi_1 \rangle}{\partial y} \quad \text{and} \quad \langle v_1 \rangle = -\frac{\partial \langle \psi_1 \rangle}{\partial x}, \tag{A27}$$

and associated vorticity $\langle \omega_1 \rangle = -\nabla^2 \langle \psi_1 \rangle$, reduces (A25) to

$$-\frac{Wo^2}{2} \text{Re} \left(\frac{\partial \Psi_0}{\partial y} \frac{\partial \Omega_0^*}{\partial x} - \frac{\partial \Psi_0}{\partial x} \frac{\partial \Omega_0^*}{\partial y} \right) = \nabla^2 \nabla^2 \langle \psi_1 \rangle, \tag{A28}$$

involving the complex functions Ψ_0 and $\Omega_0^* = -\nabla^2 \Psi_0^*$. The resulting recirculating cells can be obtained by integrating (A28) subject to the boundary conditions:

$$\langle \psi_1 \rangle = (x, y) \cdot \nabla \langle \psi_1 \rangle = 0 \quad \text{at} \quad x^2 + y^2 = 1, \quad (\text{A29})$$

$$\langle \psi_1 \rangle = 0 \quad \text{as} \quad x^2 + y^2 \rightarrow \infty. \quad (\text{A30})$$

In cylindrical polar coordinates:

$$-\frac{Wo^2}{2} \text{Re} \left[\frac{1}{r} \left(\frac{\partial \Psi_0}{\partial \theta} \frac{\partial \Omega_0^*}{\partial r} - \frac{\partial \Psi_0}{\partial r} \frac{\partial \Omega_0^*}{\partial \theta} \right) \right] = \nabla^2 \nabla^2 \langle \psi_1 \rangle. \quad (\text{A31})$$

The equation can be solved using the method of separation of variables, supposing $\langle \psi_1 \rangle = \psi_{1R}(r) \sin 2\theta$, and the method of variations of parameters to do

$$\begin{aligned} \psi_{1R}(r) = & r^4 \left(\frac{1}{48} \int_1^r \frac{1}{r'} \Phi(r') dr' + C_1 \right) - r^2 \left(\frac{1}{16} \int_1^r r' \Phi(r') dr' + C_2 \right) \\ & + \left(\frac{1}{16} \int_1^r r'^3 \Phi(r') dr' + C_3 \right) + \frac{1}{r^2} \left(-\frac{1}{48} \int_1^r r'^5 \Phi(r') dr' + C_4 \right), \end{aligned} \quad (\text{A32})$$

where

$$\begin{aligned} \Phi(r) = & iWo^2 \text{Im} \left[\frac{H_2^{(1)}(\alpha Wor)}{H_0^{(1)}(\alpha Wo)} + \frac{2}{\|H_0^{(1)}(\alpha Wo)\|^2} \right. \\ & \left. \times \left(\frac{1}{r^2} H_2^{(1)}(\alpha Wo) H_0^{(1)}(\alpha r) + H_2^{(1)}(\alpha Wor) H_0^{(1)}(\alpha Wo) \right) \right], \end{aligned} \quad (\text{A33})$$

and

$$\|H_0^{(1)}(\alpha Wo)\|^2 = \text{Re}(H_0^{(1)}(\alpha Wo))^2 + \text{Im}(H_0^{(1)}(\alpha Wo))^2.$$

The constants

$$\begin{aligned} C_1 = & -\frac{1}{48} \int_1^\infty \frac{1}{r} \Phi(r) dr, \quad C_2 = \frac{1}{16} \int_1^\infty r \Phi(r) dr, \\ C_3 = & \frac{1}{16} \int_1^\infty \frac{1}{r} \Phi(r) dr - \frac{1}{8} \int_1^\infty r \Phi(r) dr, \\ C_4 = & -\frac{1}{24} \int_1^\infty \frac{1}{r} \Phi(r) dr + \frac{1}{16} \int_1^\infty r \Phi(r) dr, \end{aligned} \quad (\text{A34})$$

are determined by imposing the boundary conditions (A29) and (A30). The Lagrangian mean motion can be defined as follows:

$$\mathbf{v}_L = \langle \mathbf{v}_1 \rangle + \frac{1}{2} \text{Im}(\mathbf{V}_0 \cdot \nabla \mathbf{V}_0^*), \quad (\text{A35})$$

where $\frac{1}{2} \text{Im}(\mathbf{V}_0 \cdot \nabla \mathbf{V}_0^*)$ is the Stokes drift or correction. In the present case, the streamfunction of the Stokes drift can be calculated as follows:

$$\begin{aligned} \psi_{SD} = & \frac{1}{2} \text{Im} \left[\frac{H_2^{(1)}(\alpha Wor)}{H_0^{(1)}(\alpha Wo)} + \frac{1}{r^2} \frac{H_2^{(1)}(\alpha Wo)}{H_0^{(1)}(\alpha Wo)} \left(\frac{H_0^{(1)*}(\alpha Wor)}{H_0^{(1)*}(\alpha Wo)} - 1 \right) \right. \\ & \left. + \frac{H_0^{(1)}(\alpha Wor) H_2^{(1)*}(\alpha Wor)}{H_0^{(1)}(\alpha Wo) H_0^{(1)*}(\alpha Wo)} \right] \sin 2\theta. \end{aligned} \quad (\text{A36})$$

REFERENCES

- ¹A. A. Linninger, K. Tangen, C. Y. Hsu, and D. Frim, "Cerebrospinal fluid mechanics and its coupling to cerebrovascular dynamics," *Annu. Rev. Fluid Mech.* **48**(1), 219–257 (2016).
- ²D. H. Kelley and J. H. Thomas, "Cerebrospinal fluid flow," *Annu. Rev. Fluid Mech.* **55**, 237–264 (2023).
- ³C. Dauleac, T. Jacquesson, and P. Mertens, "Anatomy of the human spinal cord arachnoid cisterns: Applications for spinal cord surgery," *J. Neurosurg.* **31**(5), 756–763 (2019).
- ⁴H. W. Stockman, "Effect of anatomical fine structure on the flow of cerebrospinal fluid in the spinal subarachnoid space," *J. Biomech. Eng.* **128**(1), 106–114 (2006).
- ⁵H. W. Stockman, "Effect of anatomical fine structure on the dispersion of solutes in the spinal subarachnoid space," *J. Biomech. Eng.* **129**(5), 666–675 (2007).
- ⁶K. M. Tangen, Y. Hsu, D. C. Zhu, and A. A. Linninger, "CNS wide simulation of flow resistance and drug transport due to spinal microanatomy," *J. Biomech.* **48**(10), 2144–2154 (2015).
- ⁷S. H. Pahlavian, T. Yiallourou, R. S. Tubbs, A. C. Bunck, F. Loth, M. Goodin, M. Rasee, and B. A. Martin, "The impact of spinal cord nerve roots and denticulate ligaments on cerebrospinal fluid dynamics in the cervical spine," *PLoS One* **9**(4), e91888 (2014).
- ⁸M. A. Reina, A. Boezaart, C. De Andres-Serrano, R. Rubio-Haro, and J. De Andrés, *Drug Delivery Systems. Methods in Molecular Biology*, Vol. 2059 (Humana, 2020).
- ⁹A. O. Ayansiji, D. S. Gehrke, B. Baralle, A. Nozain, M. R. Singh, and A. A. Linninger, "Determination of spinal tracer dispersion after intrathecal injection in a deformable CNS model," *Front. Physiol.* **14**, 1244016 (2023).
- ¹⁰J. J. Lawrence, W. Coenen, A. L. Sánchez, G. Pawlak, C. Martínez-Bazán, V. Haughton, and J. C. Lasheras, "On the dispersion of a drug delivered intrathecally in the spinal canal," *J. Fluid Mech.* **861**, 679–720 (2019).
- ¹¹N. Riley, "Steady streaming," *Ann. Rev. Fluid Mech.* **33**(1), 43–65 (2001).
- ¹²A. L. Sánchez, C. Martínez-Bazán, C. Gutiérrez-Montes, E. Criado-Hidalgo, G. Pawlak, W. Bradley, V. Haughton, and J. C. Lasheras, "On the bulk motion of the cerebrospinal fluid in the spinal canal," *J. Fluid Mech.* **841**, 203–227 (2018).
- ¹³G. G. Stokes, "On the theory of oscillating waves," *Trans. Cambridge Philos. Soc.* **8**, 441–455 (1847).
- ¹⁴L. Rayleigh, "On the circulation of air observed in Kundt's tubes, and on some allied acoustical problems," *Philos. Trans. R. Soc. London* **175**, 1–21 (1884).
- ¹⁵J. Holtmark, I. Johnsen, T. Sikkeland, and S. Skavlem, "Boundary layer flow near a cylindrical obstacle in an oscillating, incompressible fluid," *J. Acoust. Soc. Am.* **26**(1), 26–39 (1954).
- ¹⁶K. Chong, S. D. Kelly, S. Smith, and J. D. Eldredge, "Inertial particle trapping in viscous streaming," *Phys. Fluids* **25**(3), 033602 (2013).
- ¹⁷W. P. Raney, J. C. Corelli, and P. J. Westervelt, "Acoustical streaming in the vicinity of a cylinder," *J. Acoust. Soc. Am.* **26**(6), 1006–1014 (1954).
- ¹⁸S. Skavlem and S. Tjøtta, "Steady rotational flow of an incompressible, viscous fluid enclosed between two coaxial cylinders," *J. Acoust. Soc. Am.* **27**(1), 26–33 (1955).
- ¹⁹M. Tatsuno, "Circulatory streaming around an oscillating circular cylinder at low Reynolds numbers," *J. Phys. Soc. Jpn.* **35**(3), 915–920 (1973).
- ²⁰M. Tatsuno and P. W. Bearman, "A visual study of the flow around an oscillating circular cylinder at low keulegan–carpenter numbers and low stokes numbers," *J. Fluid Mech.* **211**, 157–182 (1990).
- ²¹P. Justesen, "A numerical study of oscillating flow around a circular cylinder," *J. Fluid Mech.* **222**, 157–196 (1991).
- ²²W. Coenen, "Steady streaming around a cylinder pair," *Proc. R. Soc. A* **472**(2195), 20160522 (2016).
- ²³J. Alaminos-Quesada, J. J. Lawrence, W. Coenen, and A. L. Sánchez, "Oscillating viscous flow past a streamwise linear array of circular cylinders," *J. Fluid Mech.* **959**, A39 (2023).
- ²⁴B. R. Lutz, J. Chen, and D. T. Schwartz, "Microscopic steady streaming eddies created around short cylinders in a channel: Flow visualization and stokes layer scaling," *Phys. Fluids* **17**(2), 023601 (2005).
- ²⁵B. R. Lutz, J. Chen, and D. T. Schwartz, "Hydrodynamic tweezers: 1. Noncontact trapping of single cells using steady streaming microeddies," *Anal. Chem.* **78**(15), 5429–5435 (2006).

- ²⁶W. Tien, D. Dabiri, V. H. Lieu, and D. T. Schwartz, “Volumetric velocity measurements of an acoustic streaming microeddy array using color-coded three-dimensional micro particle tracking velocimetry,” in *PIV13; Tenth International Symposium on Particle Image Velocimetry, Delft, The Netherlands, July 2–4, 2013*.
- ²⁷A. Marin, M. Rossi, B. Rallabandi, C. Wang, S. Hilgenfeldt, and C. J. Kähler, “Three-dimensional phenomena in microbubble acoustic streaming,” *Phys. Rev. Appl.* **3**, 041001 (2015).
- ²⁸B. Rallabandi, A. Marin, M. Rossi, C. J. Kähler, and S. Hilgenfeldt, “Three-dimensional streaming flow in confined geometries,” *J. Fluid Mech.* **777**, 408–429 (2015).
- ²⁹F. K. Chan, Y. Bhosale, T. Parthasarathy, and M. Gazzola, “Three-dimensional geometry and topology effects in viscous streaming,” *J. Fluid Mech.* **933**, A53 (2022).
- ³⁰A. Mendez, R. Islam, T. Latypov, P. Basa, O. J. Joseph, B. Knudsen, A. M. Siddiqui, P. Summer, L. J. Staehnke, P. J. Grahn, N. Lachman, A. J. Windebank, and I. A. Lavrov, “Segment-specific orientation of the dorsal and ventral roots for precise therapeutic targeting of human spinal cord,” *Mayo Clin. Proc.* **96**(6), 1426–1437 (2021).
- ³¹W. Coenen, C. Gutiérrez-Montes, S. Sincomb, E. Criado-Hidalgo, K. Wei, K. King, V. Haughton, C. Martínez-Bazán, A. L. Sánchez, and J. C. Lasheras, “Subject-specific studies of CSF bulk flow patterns in the spinal canal: Implications for the dispersion of solute particles in intrathecal drug delivery,” *Am. J. Neuroradiol.* **40**(7), 1242–1249 (2019).
- ³²L. R. Sass, M. Khani, G. Natividad, R. S. Tubbs, O. Baledent, and B. A. Martin, “A 3D subject-specific model of the spinal subarachnoid space with anatomically realistic ventral and dorsal spinal cord nerve rootlets,” *Fluids Barriers CNS* **14**(1), 36 (2017).
- ³³J. Jeong and F. Hussain, “On the identification of a vortex,” *J. Fluid Mech.* **285**, 69–94 (1995).
- ³⁴S. Katsanoulis, F. Kogelbauer, R. Kaundinya, J. Ault, and G. Haller, “Approximate streamsurfaces for flow visualization,” *J. Fluid Mech.* **954**, A28 (2023).
- ³⁵W. Thielicke and E. Stamhuis, “PIVlab-towards user-friendly, affordable and accurate digital particle image velocimetry in MATLAB,” *J. Open Res. Software* **2**(1), e30 (2014).
- ³⁶J. Alaminos-Quesada, “Limit of the two-dimensional linear potential theories on the propulsion of a flapping airfoil in forward flight in terms of the Reynolds and Strouhal number,” *Phys. Rev. Fluids* **6**, 123101 (2021).
- ³⁷S. Sincomb, W. Coenen, C. Gutiérrez-Montes, C. Martínez-Bazán, V. Haughton, and A. L. Sánchez, “A one-dimensional model for the pulsating flow of cerebrospinal fluid in the spinal canal,” *J. Fluid Mech.* **939**, A26 (2022).
- ³⁸B. J. Davidson and N. Riley, “Jets induced by oscillatory motion,” *J. Fluid Mech.* **53**(2), 287–303 (1972).
- ³⁹J. Alaminos-Quesada, C. Gutiérrez-Montes, W. Coenen, and A. L. Sánchez, “Stationary flow driven by non-sinusoidal time-periodic pressure gradients in wavy-walled channels,” *Appl. Math. Modell.* **122**, 693–705 (2023).
- ⁴⁰M. Tatsuno, “Secondary flow induced by a circular cylinder performing unharmonic oscillations,” *J. Phys. Soc. Jpn.* **50**(1), 330–337 (1981).